The destabilization of shear layers by asymmetric confinement and stratification

M. R. Turner[1]

[1]School of Mathematics and Physics, University of Surrey, Guildford, Surrey GU2 7XH, UK
Corresponding author: M. R. Turner, m.turner@surrey.ac.uk

(Received xx; revised xx; accepted xx)

The absolute and convective instability properties of a parallel shear flow in a stratified fluid, confined between two parallel rigid plates is considered. The flow is assumed to be two-dimensional, inviscid and incompressible, and is modelled using both a discontinuous two-layer stratification profile and a continuous stratification profile. Significantly, it is found that asymmetrically confining the flow by the two plates, and asymmetrically positioning the density interface such that it does not occur at the centre of the shear layer, both lead to a destabilization of the flow for a range of flow parameter values, with an absolute instability occurring for an increased parameter range. We identify parameter regimes for asymmetric confinement where the destabilizing effect is strong enough to generate an absolutely unstable co-flow shear layer; this contrasts with the unconfined case for which only absolutely unstable counter-flow shear layers exist. In the semi-confined case (i.e. asymmetric confinement by one plate) it is found that the most unstable scenario occurs when the plate is placed in the faster/lighter stream. The robustness of the results found for a discontinuous density interface are confirmed using a continuous density profile. These results give valuable new insight into a class of flows such as co-axial injectors for high-speed fluid atomization.

1. Introduction

The stability properties of a sheared, density-stratified environment is significant because, unstable shear layers can lead to nonlinear overturning waves propagating along the density interface producing turbulence and mixing (Carpenter *et al.* 2010), and ultimately atomization in two-phase flows (Lasheras *et al.* 1998; Lefebvre & McDonell 2017). Understanding when and where turbulence and mixing occur in shear layers is important in engineering systems such as fuel mixing in combustion engines (Juniper & Candel 2003; Sirignano 2021), potentially making them more efficient; in the aerospace and marine industry where shear layers generate drag and noise, and controlling turbulence, via methods such as compliant surfaces, can improve performance and fuel efficiency (Weilgart 2018; Poole & Turner 2023); and environmental flows where the mixing of weather patterns or pollutants can affect climate modelling and environmental monitoring (Peltier & Caulfield 2003; Caulfield 2021). Calculating the stability of such shear layers

has a long history going back to Helmholtz (1868) and Kelvin (1871) for two-dimensional homogeneous and stratified shear layers respectively. Since these initial works, various authors have considered variations to these problems, making the problem more complex, but each time focusing on understanding the basic instability mechanism and how it might be exploited and controlled.

In this paper our focus is on calculating the transition point from convective to absolutely unstable flows. A convectively unstable flow is one where instability modes grow and propagate away from the source of the disturbance (either upstream or downstream), while an absolutely unstable flow has instability modes which propagate both upstream and downstream from the disturbance source. An important feature of an absolute instability is that it can lead to a global instability which can dominate and fill the whole flow domain, and in fact for a strictly parallel flow, an absolute instability is equivalent to a global instability. The first significant study of absolute instability in the hydrodynamic context was Huerre & Monkewitz (1985) who showed the unconfined homogeneous shear layer was absolutely unstable. This work was extended by Triantafyllou (1994) to include a discontinuous step in density between the two layers. The initial work by Huerre & Monkewitz (1985) has inspired a huge array of studies on this problem, producing a vast literature. However, the effect of flow asymmetries on the stability of a stratified shear layer has received little attention, but is of interest in engineering shear flows including high-speed jets.

The shear layer we consider consists of two fluids flowing parallel to the x-axis, is two-dimensional, with dimensional velocities $U_1^*\mathbf{e}_x$ and $U_2^*\mathbf{e}_x$ far from the shear layer, and we non-dimensionalize our problem with the typical velocity scale $\frac{1}{2}(U_1^* + U_2^*)$. This gives us a dimensionless basic velocity profile $U(y)\mathbf{e}_x$ of the form

$$U(y) = 1 + rf(y), \tag{1.1}$$

where y is a variable in the cross-stream direction, $\lim_{y\to\pm\infty} f(y) = \pm 1$ and

$$r = \frac{U_1^* - U_2^*}{U_1^* + U_2^*},$$

is the shear flow parameter. Note, in this formulation we remain in the fixed inertial frame of reference, rather than converting to a moving frame. This is because the focus of this work is on classifying absolutely and convectively unstable flow parameter regimes, and this distinction would become more confusing if the parameter dependent speed of the moving frame needs to be taken into account. In the fixed inertial frame, an absolute instability is an instability which has zero group velocity. The two fluids have densities ρ_1 and ρ_2 with the density ratio defined by $S = \rho_2/\rho_1 > 1$, such that the flow is stably stratified. The dimensionless position variables (x, y) are non-dimensionalized on a convenient measure of the shear layer thickness, L. When $|r| < 1$, U_1^* and U_2^* have the same sign, we call this a *co-flow shear layer*, while when $|r| > 1$, U_1^* and U_2^* are of opposite sign and we call this a *counter-flow shear layer*. The flow is a parallel flow, i.e. the base flow only depends on the cross-stream variable y, and so any absolute instability also implies a global instability. For $f(y) = \tanh(y/2)$, Huerre & Monkewitz (1985) found that for strong counter flows, the flow is absolutely unstable, and convectively unstable otherwise, with the transition at $r = 1.315$. However Huerre & Monkewitz (1985) were only considering an unconfined shear layer, and Healey (2009) showed that confinement of the shear layer between two parallel plates is significant to the absolute instability properties of the flow, with the biggest absolute instability effects produced by asymmetric confinement.

The mathematical justification showing the importance of confinement comes from the challenge of applying spatio-temporal stability analysis together with the Briggs method

(Briggs 1964). In this theory the initial value problem is solved using an impulse disturbance and taking Fourier transforms in x and Laplace transforms in time t. The resulting solution is hence an inverse Fourier-Laplace transform, which using the method of steepest descent in the large t limit, can be written as a Fourier integral over α, the streamwise wavenumber. The absolute instability properties can then be determined by deforming the Fourier inversion contour through special saddle points in the complex α-plane which link both upstream and downstream propagating wavepackets. The dominant saddle is the one with the largest $\mathrm{Im}(\omega)$, where ω is the disturbance angular frequency, and is known as a *pinch point*, when we use the wave-form convention $\exp(\mathrm{i}(\alpha x - \omega t))$ in (2.2)-(2.4). For unbounded shear layers, with exponential decay as $y \to \pm\infty$, the dominant saddle lies in the quadrant $\mathrm{Re}(\alpha) > 0$, $\mathrm{Im}(\alpha) < 0$, and a branch cut lies along the negative imaginary α-axis. However, when the flow is confined by rigid plates, the decaying solution is replaced by a no-penetration condition at the plate (for inviscid flows) which generates an infinite number of discrete poles and saddle points close to the imaginary α-axis. The addition of these additional saddle points makes identifying the dominant pinch point challenging, but Healey (2009) showed that these saddles can become the dominant saddle under certain flow conditions. Healey also showed, building on his works on the rotating disc boundary layer (Healey 2006*a*,*b*, 2007) that confinement of shear layers can cause modes which are convectively unstable in the cross-flow direction, y, to become absolutely unstable modes. This occurs when the dominant mode in the unbounded problem crosses the imaginary α-axis to a region where the wavepacket grows exponentially in a direction with a cross-flow direction component, but the rigid plate enforces a zero boundary condition and thus the mode travels back to the shear layer, setting up the absolute instability. This phenomena also allows the absolute instability to persist even when the plate is moved arbitrarily far from the shear layer. This same behaviour is seen for other flows such as planar jets and wakes (Yu & Monkewitz 1990; Taylor & Peake 1999; Juniper 2006, 2007, 2008) and swirling jets (Lim & Redekopp 1998; Healey 2008).

When stratified shear flows are observed in laboratory experiments (Koop & Browand 1979; Lawrence *et al.* 1991), they often exhibit some form of asymmetry. This asymmetry can take the form of asymmetric confinement above or below the shear layer, a displaced density interface from the centre of the shear layer, or asymmetric velocity profiles. In this work we focus on asymmetric confinement and a displaced density interface. Healey (2009) showed for the homogeneous shear layer that for temporal instabilities, asymmetric confinement is the most stable configuration, followed by symmetric confinement, semi-confinement and then unconfined flows. However, he showed that for the absolute instability it is the asymmetric confined configuration which is most unstable. The series of experiments by Matas (2015); Matas *et al.* (2018); Bozonnet *et al.* (2022) for an air-water shear layer confirm the findings of Healey (2009) by showing that asymmetric confinement can generate an absolute instability in flow regimes, which, when unconfined, are convectively unstable. Stratified shear layers in the ocean are not immediately applicable to the results in this paper, because in these cases the density stratification between the upper and lower oceans is about $S \approx 1$. However, what is significant is that in these flows the effect of displacing the shear interface away from the centre of the shear layer has been studied. Varying the location of this point generates significant differences in the form of the nonlinear waves which are generated on the interface surface (Lawrence *et al.* 1991; Caulfield *et al.* 1995; Carpenter *et al.* 2010), and Danyi (2018) found that displacing the mean density position with respect to the position of the shear layer can destabilize the flow, even if the stratification is a stable stratification. In the current paper our results will focus on the effect of varying the density interface position in high-speed jet flows with $S \geq 1$.

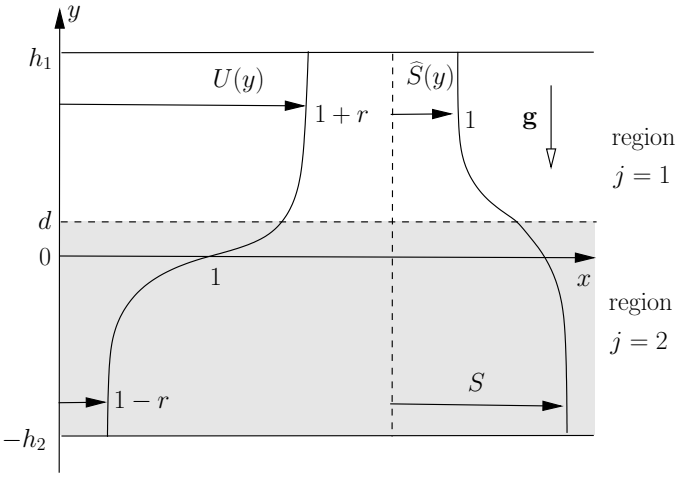

Figure 1. Schematic of the shear layer problem we consider. The density stratification is assumed to be stable, so $S \geq 1$, and the shear rate, r, can be positive or negative.

In the current paper we derive the governing equations in §2 and examine the neutral curves for the temporal stability for confined shear layers in §3. In §4 we derive the long-wavelength dispersion relations for comparison with full numerical results in §5 for symmetrically confined shear layers and §6 for asymmetrically confined shear layers. In §6 we also consider the absolute instability of semi-confined shear layers (asymmetrically confined by a single plate) and give a simple mechanism for the stability hierarchy identified. Comparison of the results in §5 and 6 for a continuous density profile is considered in §7, confirming the robustness of the results previously identified. Conclusions are given in §8.

2. Governing equations

The shear layer problem considered in figure 1 is assumed to be inviscid and irrotational and thus the governing equations are the two-dimensional non-dimensionalised Euler equations

$$\frac{\partial \mathbf{u}}{\partial t} + \mathbf{u}\cdot\nabla\mathbf{u} = -\frac{1}{\rho}\nabla\widehat{p} - F^{-2}\mathbf{e}_y, \qquad \nabla\cdot\mathbf{u} = 0, \qquad \frac{\partial \rho}{\partial t} + \mathbf{u}\cdot\nabla\rho = 0, \tag{2.1}$$

where $F = (U_1^* + U_2^*)/(2\sqrt{gL})$ is the Froude number, $\mathbf{e}_y$ is a unit vector in the y-direction and g is the gravitational constant. Here $\mathbf{u} = (\widehat{u}, \widehat{v})$ are the velocity components in the x and y directions, and $\widehat{p}$ is the pressure. The function $\widehat{S}(y)$ is the non-dimensional density profile, and is assumed to vary only in the cross-flow direction. The flow is confined above and below by rigid parallel plates at $y = h_1$ and $y = -h_2$.

The form of the governing stability equations come from seeking two-dimensional normal-mode disturbances to the basic parallel velocity profile $\mathbf{u} = U(y)\mathbf{e}_x$ of the form

$$\mathbf{u} = (\widehat{u}(x,y,t), \widehat{v}(x,y,t)) = (U(y), 0) + \widehat{\delta}(u(y), v(y))\exp\left[\mathrm{i}(\alpha x - \omega t)\right], \tag{2.2}$$

$$\widehat{p}(x,y,t) = P_0 - \int \widehat{S}(y)F^{-2}\,\mathrm{d}y + \widehat{\delta}p(y)\exp\left[\mathrm{i}(\alpha x - \omega t)\right], \tag{2.3}$$

$$\rho(x,y,t) = \widehat{S}(y) + \widehat{\delta}\sigma(y)\exp\left[\mathrm{i}(\alpha x - \omega t)\right], \tag{2.4}$$

where $0 < \widehat{\delta} \ll 1$ is a small parameter which allows for linearization and P_0 is a constant. The disturbances are wave-like disturbances with wavenumber α and angular frequency

$\omega = \alpha c$, where c is the phase speed. Substituting these forms into (2.1) and linearizing leads to the system of equations

$$\begin{aligned} \mathrm{i}\alpha u + v' &= 0, && (2.5)\\ -\mathrm{i}\omega u + \mathrm{i}\alpha U u + U' v &= -\mathrm{i}\alpha \frac{p}{\widehat{S}}, && (2.6)\\ -\mathrm{i}\omega v + \mathrm{i}\alpha U v &= -\frac{p'}{\widehat{S}} - F^{-2}\frac{\sigma}{\widehat{S}}, && (2.7)\\ -\mathrm{i}\omega\sigma + \mathrm{i}\alpha U\sigma + v\widehat{S}' &= 0, && (2.8) \end{aligned}$$

where the dash denotes a derivative with respect to y. Eliminating the quantities u, σ and p from these equations leads to a modified Taylor-Goldstein equation

$$(\alpha U - \omega)(v'' - \alpha^2 v) - \alpha U'' v + \frac{\widehat{S}'}{\widehat{S}}\left[(\alpha U - \omega)v' - \alpha U' v - \frac{\alpha^2 F^{-2}}{(\alpha U - \omega)}v\right] = 0, \qquad (2.9)$$

with the inertia terms retained (Drazin & Reid 1981; Drazin 2002). Here $F^{-2}\widehat{S}'/\widehat{S}$ is the Richardson number, a measure of the buoyancy to shear in the system. This equation is solved with the appropriate boundary conditions, which for h_1 or h_2 finite are

$$v(h_1) = v(-h_2) = 0, \qquad (2.10)$$

while for h_1 or h_2 infinite

$$v'(h_1) + \alpha v(h_1) = v'(-h_2) - \alpha v(-h_2) = 0, \qquad (2.11)$$

gives the correct exponential decay at $y = \pm\infty$, when $\mathrm{Re}(\alpha) > 0$. It should also be noted that in this case we also require the wave to be unstable, i.e. $\omega_i > 0$. In the case when the mode decays in time $\omega_i < 0$, then the causal solutions could involve exponential growth in the far field (Le Dizès & Billant 2009; Riedinger *et al.* 2010; Zuccoli *et al.* 2024). When using (2.11) in numerical calculations, h_1 and h_2 need to be chosen large enough such that the eigenmode is in the correct exponential decay regime, and we find a value of $h_1 = h_2 = 20$ sufficient to guarantee this for the results in this paper.

In sections 3 to 6 we consider a discontinuous density profile which consists of jump in density at $y = d$, and so in this case $\widehat{S}(y)$ takes the form

$$\widehat{S}(y) = \begin{cases} 1 & y \geq d \\ S & y < d \end{cases}, \qquad (2.12)$$

with $S \geq 1$ so that the stratification is stable. This profile is a model for the scenario of two immiscible fluids in the shear layer, such as the breakup of liquid-liquid jets (Kitamura *et al.* 1982; Richards *et al.* 1994; Homma *et al.* 2006) or the breakup of liquid jets in a co-axial injector (Juniper & Candel 2003; Juniper 2006). In this case we require two jump conditions at $y = d$ to ensure we have continuity of the normal displacement of the fluids, and the continuity of pressure at the density interface, which are given by

$$\left[\frac{v}{\alpha U - \omega}\right]_{y=d} = 0 \quad \text{and} \quad \left[\widehat{S}\left\{(\alpha U - \omega)v' - \alpha U' v - \frac{\alpha^2 F^{-2}}{(\alpha U - \omega)}v\right\}\right]_{y=d} = 0, \qquad (2.13)$$

where $[\cdot]_{y=d} \equiv \lim_{y\to d^+}[\cdot] - \lim_{y\to d^-}[\cdot]$ (Pouliquen *et al.* 1994; Schmid & Henningson 2001).

The form of the basic shear layer flow we consider is given by (1.1). The flow shear rate, r, can be positive or negative and this change corresponds to the faster stream being in

the lighter or heavier fluid respectively. In this paper we will present new theoretical and numerical results on the temporal stability of a general shear layer where f in (1.1) is a general anti-symmetric function with the required properties, and illustrate these findings specifically for the tanh shear layer where

$$f(y) = \tanh\left(\frac{y}{2}\right). \tag{2.14}$$

The absolute instability results will solely be focused on the tanh shear layer.

In the results we present, our interest is in considering a fixed anti-symmetric velocity profile (1.1) with $f(y) = -f(-y)$, for varying r, but then breaking the remaining symmetry of the flow by considering both asymmetric confinement $h_1 \neq h_2$ and by considering a density jump which is asymmetric about $y = 0$, i.e. $d \neq 0$ in (2.12). This second case has been observed in the ocean scenario (Anni & Farmer 1988; Wesson & Gregg 1994; Yoshida *et al.* 1998; Tedford *et al.* 2009) as well as in the laboratory (Koop & Browand 1979; Lawrence *et al.* 1991).

2.1. *Potential effects of viscosity*

In this work, we have considered a shear layer model where viscosity is neglected. In a truly inviscid problem this is a valid assumption, but we briefly consider the consequences of the presented results when a small, finite viscosity is considered. One major feature missing in the inviscid problem is boundary layers at the plates. Typically boundary layer instabilities are weaker than shear layer instabilities, so if the boundary layers at the plate are thin, which they usually are in large-Reynolds number shear flows such as those we are interested in, their influence should be minimal. Rienstra & Darau (2011) showed for a simple piecewise linear boundary layer next to an impedance wall that the most absolutely unstable scenario is the inviscid, zero thickness boundary layer. A stabilizing effect on the absolute instability for moderate Reynolds numbers was also found for jets and wakes by Juniper *et al.* (2011) and Tammisola *et al.* (2011) and for a swirling jet flow by Tammisola & Juniper (2016). They concluded that for strong symmetric confinements, the boundary layers at the plates can begin to interfere with the shear layers, leading to an enhanced stabilization of the flow. In the current work the majority of the confinements we consider are weak and moderate, hence we expect our results to be relevant for large and moderate Reynolds number flows.

The addition of weak viscosity would also lead to a diffusion of mass and momentum between the two-fluids at the interface, by imposing continuous tangential stress. This effect would act to smooth out the density jump at the interface, as well as modifying both it, and the velocity profile, into asymmetric configurations which are no longer anti-symmetric about $y = 0$. The smoothed purely anti-symmetric form of the density profile is considered in §7, but the asymmetric forms are not considered, despite them being observed in experimental setups (Ouro *et al.* 2019). Healey (2009) showed for a homogeneous shear layer that an asymmetric velocity profile can be destabilizing, in a symmetrically confined system, but the confinement had to be strong, and the asymmetric velocity profile carefully chosen to achieve this. Thus asymmetric confinement in the homogeneous case has a much more significant effect on the absolute instability and we expect this to also be the case for the stratified problem we consider here.

3. Temporal stability of confined shear layers

The theoretical results we present here are concerned with the position of the neutral curve as confinement parameters are varied, for fixed system parameters S, d, r, F^{-2}. Along the

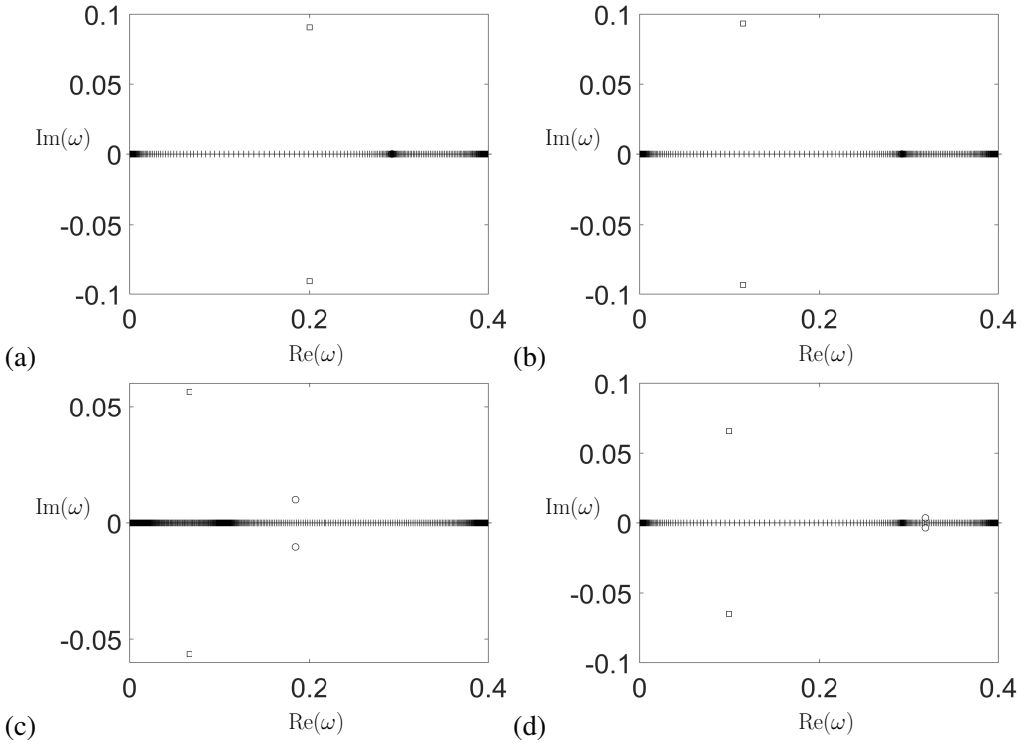

Figure 2. Global eigenvalues $\omega = \alpha c$ for the tanh shear layer with $\alpha = 0.2$ and $r = 1$ for (a) $S = 1$ and $S = 5$ with (b) $(F^{-2}, d) = (0, 1)$, (c) $(F^{-2}, d) = (0, -1)$ (d) $(F^{-2}, d) = (0.075, 1)$. In each case $h_1 = h_2 = 10$. The modes denoted by the squares (Kelvin-Helmholtz modes) eventually become neutral at a finite value of α, while in (c) and (d) the circle modes (internal modes) persist to large α values. The modes along the $\mathrm{Re}(\omega)$ axis are a discrete representation of the continuous spectrum.

neutral curve $c = \omega/\alpha = c_r + \mathrm{i}c_i$ is purely real ($c_i = 0$) and we seek the value of $\alpha \in \mathbb{R}$ at the point where c_i first equals 0. Inside the neutral curves $c \in \mathbb{C}$ and to determine information about growth rates, c_i, for such disturbances requires a numerical solution of (2.9).

Before going on to explore theoretical results on the temporal stability neutral curve of these stratified shear flows, we motivate our analysis by considering the global temporal eigenvalue structure, inside the neutral curve ($c_i \neq 0$), for the tanh shear layer for the value $\alpha = 0.2$ and $r = 1$ for the cases (a) $S = 1$ and $S = 5$ with (b) $(F^{-2}, d) = (0, 1)$, (c) $(F^{-2}, d) = (0, -1)$, (d) $(F^{-2}, d) = (0.075, 1)$ in figure 2. In each case the flow is symmetrically confined with $h_1 = h_2 = 10$. The numerical scheme for this calculation, solving (2.9), is based on collocation with Chebyshev polynomials and is given in § A of the supplementary material. The density ratio $S = 5$ is akin to that used in the experiments of Strykowski & Niccum (1992), who used air and sulfur hexafluoride as two fluids to examine the stability of spatially developing mixing layers.

Here, as we are looking at the temporal stability inside the neutral curve, $\alpha \in \mathbb{R}$, and the flow is inviscid, so the temporal eigenvalues $c = c_r + \mathrm{i}c_i$ are either real or complex conjugate pairs for unstable modes. The result for $S = 1$ in figure 2 shows the stability of the homogeneous shear layer, and here the unstable modes, represented by the squares, are the Kelvin-Helmholtz (KH) modes which are driven by the form of the shear layer. When we consider $S > 1$ with $d > 0$ in panel (b), we again only observe the one unstable KH mode, but in panel (c), where $S > 1$ with $d \leq 0$, i.e. the centre of the shear layer occurs in

the lighter of the two fluids, the flow has two unstable modes. Following both these modes while increasing α we find that the modes represented by squares are again KH modes and eventually become neutral at a point where ($c_r = 1$), while the modes identified by the circles remain unstable to large values of α (i.e. the short-wave limit). These modes indicated by the circles are internal modes, with their eigenmodes concentrated at the density interface. In the zero Richardson number limit ($F^{-2} = 0$) these internal modes are only unstable when $d \leq 0$, but when $F^{-2} \neq 0$, in panel (d), they can be shown to also be unstable for $d > 0$. The KH modes have the nice property that they become neutrally stable at a value of α where $c = 1$, and hence we are able to give theoretical results for these modes in §3.1, while for the internal modes we are restricted to examining these numerically (except for the $F^{-2} = 0$ limit) in §3.3. While we examine the properties of these two mode types separately, we note that the full flow structure can only be known if properties of both modes are considered, when they are both unstable. As the main interest in the paper is in high speed jet flows, i.e. small Richardson numbers, we expect the $F^{-2} = 0$ results to be informative of these flows, with the $0 < F^{-2} \ll 1$ results being a perturbation on these results. Note, while our interest in the $F^{-2} \ll 1$ case, we choose to use moderately large values of F^{-2} such that its non-zero effect can be observed graphically.

The numerical global eigenvalue results for the stratified KH modes have the same structure as those observed in the homogeneous shear layer in Healey (2009). These neutral waves have a critical point at $y = y_c$ which occurs where $U(y_c) = c$, which coincides with the inflection point of the flow, $U'' = 0$. If we assume that f is anti-symmetric and $f(-y) = -f(y)$ this implies that $y_c = 0$ and thus $c = 1$ at the neutral curve, as we observed numerically earlier. The Taylor-Goldstein equation (2.9) then reduces in each fluid to the Rayleigh equation

$$f(v'' - \alpha^2 v) - f''v = 0, \tag{3.1}$$

with the matching conditions across the density jump at $y = d$

$$\left[\frac{v}{f}\right]_{y=d} = 0, \quad \left[\widehat{S}\left(fv' - f'v - \frac{J_0}{(S-1)f}v\right)\right]_{y=d} = 0, \tag{3.2}$$

where

$$J_0 = \frac{(S-1)F^{-2}}{r^2},$$

is a local Richardson number and $\widehat{S}$ is given by (2.12). Here we have chosen to include the $(S-1)$ factor in the definition of J_0 to simplify the form of the results presented in this section. The above system with the appropriate boundary conditions gives an eigenrelation, in terms of the system parameters, along the neutral curve. We note that the form of the neutral curve is not directly dependent on r, but is only a function of r via J_0. However, the unstable growth rates are directly dependent on r as we will show later. We will first consider results in the long-wave limit, when α is small, for a general anti-symmetric flow, before applying these results to the tanh shear layer profile.

3.1. *Confinement effects in the long-wave limit for the KH mode*

We can investigate the position of the intercept of the neutral curve with $\alpha = 0$ by noting that when $\alpha = 0$, $v = v_A = f$ is a solution of (3.1) as shown by Michalke (1964). Healey (2009) then showed that by writing $v = v_B = f(y)V(y)$ a second linearly independent solution can be found. The general solution in each fluid is then a linear combination of these solutions, namely

$$v_j = A_j f(y) + B_j f(y)V(y),$$

where

$$V(y) = \int \frac{1}{f(t)^2}\,\mathrm{d}t,$$

for arbitrary constants A_j, B_j with $j = 1, 2$ as per the notation in figure 1. Satisfying the boundary conditions $v_1(h_1) = v_2(-h_2) = 0$ for the case of asymmetric confinement in each layer, leads to the two solutions

$$v_1(y) = B_1 f(y)\left[\int_{h_1}^{y} g(t)\,\mathrm{d}t + \frac{1}{f'(0)^2}\left(\frac{1}{h_1} - \frac{1}{y}\right)\right], \tag{3.3}$$

$$v_2(y) = B_2 f(y)\left[\int_{-h_2}^{y} g(t)\,\mathrm{d}t - \frac{1}{f'(0)^2}\left(\frac{1}{h_2} + \frac{1}{y}\right)\right], \tag{3.4}$$

where

$$g(t) = \frac{1}{f(t)^2} - \frac{1}{f'(0)^2 t^2}. \tag{3.5}$$

Matching these two solutions at the density jump $y = d \neq 0$ and seeking a non-trivial solution, leads to the condition

$$\begin{aligned} &SI(h_1) - I(-h_2) + \frac{1}{f'(0)^2}\left(\frac{1-S}{d} + \frac{h_1 + Sh_2}{h_1 h_2}\right) \\ &-J_0\left[I(h_1) + \frac{1}{f'(0)^2}\left(\frac{1}{h_1} - \frac{1}{d}\right)\right]\left[I(-h_2) - \frac{1}{f'(0)^2}\left(\frac{1}{h_2} + \frac{1}{d}\right)\right] = 0, \end{aligned} \tag{3.6}$$

where

$$I(\xi) = \int_{\xi}^{d} g(t)\,\mathrm{d}t.$$

Due to its construction, condition (3.6) is an eigenrelation for the parameters h_1, h_2, d, S, J_0, where given four of these parameters, the fifth can be identified such that the neutral curve intercepts $\alpha = 0$. The case $d = 0$, i.e. when the inflexion point and the density jump coincide is a non-trivial special case which is not captured by this theory, and needs to be dealt with numerically. We will see in §5 that asymmetric configurations away from this special case can be significant on the flow's absolute instability properties.

For the case of symmetric confinement when $h_1 = h_2 = h$ (3.6) becomes

$$\begin{aligned} &SI(h) - I(-h) + \frac{1}{f'(0)^2}\left(\frac{1-S}{d} + \frac{(1+S)}{h}\right) \\ &-J_0\left[I(h) + \frac{1}{f'(0)^2}\left(\frac{1}{h} - \frac{1}{d}\right)\right]\left[I(-h) - \frac{1}{f'(0)^2}\left(\frac{1}{h} + \frac{1}{d}\right)\right] = 0. \end{aligned} \tag{3.7}$$

For a homogeneous shear layer, Healey (2009) showed that this scenario is a local minimum of the plate separation, i.e. that the symmetric confinement case is locally the most unstable flow configuration. In the case of the KH mode in an inhomogeneous shear layer this is not always the case, as we now discuss.

Consider an almost symmetric configuration with h_2 close to h with d, S and J_0 fixed, then we can solve (3.6) for h_1 along the neutral curve. Therefore by writing

$$h_2 = h + \delta, \tag{3.8}$$

$$h_1 = h + h_{11}\delta + h_{12}\delta^2 + O(\delta^3), \tag{3.9}$$

where $|\delta| \ll 1$ is a small parameter (not to be confused with $\widehat{\delta}$ used in (2.2)-(2.4)), we can substitute this into (3.6) and equate like powers of δ. Substituting into (3.6), using the asymptotic result

$$\begin{aligned}\int_{a+b}^{a} g(t)\,\mathrm{d}t &= \int_{a+b}^{a}\left(g(a)+g'(a)(t-a)+\frac{1}{2}g''(a)(t-a)^2+O\left((t-a)^3\right)\right)\mathrm{d}t,\\ &= -g(a)b+\frac{1}{2}g'(a)b^2-\frac{1}{6}g''(a)b^3+O(b^4),\end{aligned}$$

for $|b| \ll 1$, and noting that as $f(t)$ is an odd function then $g(t)$ is an even function such that $g(-t) = g(t)$ and $g'(-t) = -g'(t)$, we derive (3.7) at $O(1)$,

$$-\frac{(1+Sh_{11})}{f(h)^2}-J_0 f(h)^2\left[I(h)+\frac{1}{f'(0)^2}\left(\frac{1}{h}-\frac{1}{d}\right)\right]+h_{11}\left[I(-h)-\frac{1}{f'(0)^2}\left(\frac{1}{h}+\frac{1}{d}\right)\right]=0,$$

at $O(\delta)$ and

$$\begin{aligned}&\left[-S+J_0\left[I(-h)-\frac{1}{f'(0)^2}\left(\frac{1}{h}+\frac{1}{d}\right)\right]\right]h_{12}\\ &+\left[S\frac{f'(h)}{f(h)}-J_0\left[I(-h)-\frac{1}{f'(0)^2}\left(\frac{1}{h}+\frac{1}{d}\right)\right]\right]h_{11}^2\\ &+\frac{J_0}{f(h)^2}+\frac{f'(h)}{f(h)}+\frac{f'(h)}{f(h)}J_0\left[I(h)+\frac{1}{f'(0)^2}\left(\frac{1}{h}-\frac{1}{d}\right)\right]=0,\end{aligned}$$

at $O(\delta^2)$.

At leading order the symmetrically confined case (3.7) is satisfied, while at higher orders these equations can be solved for h_{11} and h_{12}. In order to highlight the qualitative behaviour of this analysis we consider the zero local Richardson number, $J_0 = 0$ case, with the $J_0 \neq 0$, $|J_0| \ll 1$ case having qualitatively similar behaviour, as we will demonstrate for the tanh mixing layer in §3.2. With $J_0 = 0$ we find at $O(\delta)$

$$h_{11} = -\frac{1}{S},$$

while at $O(\delta^2)$

$$h_{12} = \frac{(1+S)}{S^2}\frac{f'(h)}{f(h)}.$$

Therefore

$$h_1 = h-\frac{\delta}{S}+\frac{(1+S)}{S^2}\frac{f'(h)}{f(h)}\delta^2+O(\delta^3). \tag{3.10}$$

This means the plate separation distance for neutral waves for slightly asymmetrically confined flows is

$$h_1+h_2 = 2h+\frac{S-1}{S}\delta+\frac{1+S}{S^2}\frac{f'(h)}{f(h)}\delta^2. \tag{3.11}$$

For the homogeneous case ($S = 1$) from Healey (2009) this quantity is always larger than the symmetric case which showed that the asymmetric case was always less unstable than the corresponding symmetric case for a monotonically increasing f.

For the inhomogeneous case here, there is an additional term at $O(\delta)$. The significance of this term is, if $\delta > 0$, i.e. moving both plates apart (while remaining on the neutral curve), then the symmetrically confined case is more temporally unstable than the asymmetric case. However, if $\delta < 0$ (and sufficiently small), i.e. both plates are moved together (while

remaining on the neutral curve), then the asymmetrically confined flow can be more temporally unstable than the symmetrically confined counterpart. The interesting feature of this result is that it is independent of the position of the fixed density jump $y = d$.

Note that when $\delta < 0$, the $O(\delta)$ term in (3.11) is negative, but the $O(\delta^2)$ term is positive. This combination of terms ultimately becomes positive for $\delta < \delta_c$ where

$$\delta_c = S\frac{1-S}{1+S}\frac{f(h)}{f'(h)}.$$

Thus for particularly small confinement asymmetries the flow is more unstable than the symmetric case, but for large confinement asymmetries the flow is ultimately more stable than the symmetric configuration. This is shown numerically for the tanh shear layer in §3.2.

For the case of semi-confined flows we cannot simply let h_1 or h_2 tend to ∞, as the integrals are not convergent. Also, in the unbounded half of the domain, we expect the behaviour $v_1 \sim \exp(-\alpha y)$ or $v_2 \sim \exp(\alpha y)$ respectively, but we expect these forms in the limit of small α, hence we expect $v_1 \sim 1 - \alpha y$ or $v_2 \sim 1 + \alpha y$ and we use these to fix the arbitrary constants A_1, B_1 and A_2, B_2 respectively. Note, here we are considering the limit $\alpha \to 0$, whereas in (3.3) and (3.4) we were able to consider $\alpha = 0$ directly. This then gives the expressions

$$v_1(y) = f(y)\left[1 - \alpha y - \alpha\int_{\infty}^{y}(g(t)-1)\,\mathrm{d}t + \frac{\alpha}{f'(0)^2 y}\right], \tag{3.12}$$

$$v_2(y) = f(y)\left[1 + \alpha y + \alpha\int_{-\infty}^{y}(g(t)-1)\,\mathrm{d}t - \frac{\alpha}{f'(0)^2 y}\right], \tag{3.13}$$

for an unbounded region above the shear layer and an unbounded region below the shear layer respectively. Thus the semi-confined relations can be found by matching (3.12) with (3.4) and matching (3.13) and (3.3) which lead to the expressions

$$\alpha\left[I(-h_2) - \frac{1}{f'(0)^2}\left(\frac{1}{h_2}+\frac{1}{d}\right)\right] = -\left[S + J_0\left[I(-h_2) - \frac{1}{f'(0)^2}\left(\frac{1}{h_2}+\frac{1}{d}\right)\right]\right]\left[1 - \alpha d - \alpha\int_{\infty}^{d}(g(t)-1)\,\mathrm{d}t + \frac{\alpha}{f'(0)^2 d}\right], \tag{3.14}$$

$$\alpha S\left[I(h_1) + \frac{1}{f'(0)^2}\left(\frac{1}{h_1}-\frac{1}{d}\right)\right] = \left[1 + J_0\left[I(h_1) + \frac{1}{f'(0)^2}\left(\frac{1}{h_1}-\frac{1}{d}\right)\right]\right]\left[1 + \alpha d + \alpha\int_{-\infty}^{d}(g(t)-1)\,\mathrm{d}t - \frac{\alpha}{f'(0)^2 d}\right], \tag{3.15}$$

for flows bounded below and above respectively. To find the asymptotic forms of these expressions we write $\alpha = \alpha_0 + h_2\alpha_1$ in (3.14) and $\alpha = \alpha_0 + h_1\alpha_1$ (3.15) and consider the limits $h_2 \to 0$ and $h_1 \to 0$ respectively. These lead to

$$\alpha = \frac{J_0}{1+J_0 D_+} + \frac{f'(0)^2}{(1+J_0 D_+)^2}\left[S(1+(J_0-1)D_+) - (J_0-1)(J_0 D_+ + 1)C\right]h_2 + O(h_2^2),$$

$$\alpha = \frac{J_0}{S-J_0 D_-} + \frac{f'(0)^2}{(S-J_0 D_-)^2}\left[S - (J_0-1)(J_0 D_- - S)C - (J_0-1)D_-\right]h_1 + O(h_1^2),$$

where

$$C = \int_0^d g(t)\,\mathrm{d}t - \frac{1}{f'(0)^2 d}, \quad D_\pm = d + \int_{\pm\infty}^{d}(g(t)-1)\,\mathrm{d}t - \frac{1}{f'(0)^2 d}.$$

We again highlight the asymptotic forms of these eigenrelations for the case $J_0 = 0$ which simplify to

$$\alpha \sim Sf'(0)^2 h_2, \tag{3.16}$$

and

$$\alpha \sim \frac{1}{S} f'(0)^2 h_1, \tag{3.17}$$

respectively. Both of these expressions are in a form similar to that found for the homogeneous shear layer in Healey (2009).

3.2. *Confinement effect on the tanh shear layer for KH modes*

The general long-wave results of the last section will be illustrated in this section for the smooth tanh shear layer with $f(y)$ given in (2.14). This flow field provides a convenient flow model on which to examine both temporal and absolute instability properties due to the fact that some analytic solutions can be derived. The profile has been used in the study by Huerre & Monkewitz (1985) to examine the absolute instability of an unconfined shear layer, in Healey (2009) to examine the absolute instability of asymmetrically confined homogeneous shear layers and in Carpenter *et al.* (2010) to examine the instability of stratified shear layers to name a few.

With the form of $f(y)$ given by (2.14), Michalke (1964) showed that on the neutral curve, (3.1) exhibits an exact solution. Therefore in our two layers $j = 1, 2$ we can write the general solution for the eigenmode on the neutral curve as

$$v_j(y) = A_j \left[2\alpha \cosh(\alpha y) - \sinh(\alpha y) \tanh\left(\frac{y}{2}\right)\right] + B_j \left[2\alpha \sinh(\alpha y) - \cosh(\alpha y) \tanh\left(\frac{y}{2}\right)\right], \tag{3.18}$$

where A_j, B_j give 4 unknown constants which are fixed by the two boundary conditions and the two matching conditions at the density jump. The boundary conditions at the confining plates are again $v(h_1) = v(-h_2) = 0$ while if the flow is unconfined then the condition becomes (2.11) which is equivalent to $v(\pm\infty) = 0$.

Unlike the homogeneous case in Healey (2009) there are no simple closed forms for the relations which link α, h_1, h_2, d, S and J_0. However, we can succinctly write down the forms of the neutral curve eigenconditions by introducing the following functions

$$\begin{aligned}
T_1(\xi) &= 2\alpha - \tanh(\alpha\xi) \tanh\left(\frac{\xi}{2}\right), \quad T_2(\xi) = 2\alpha \tanh(\alpha\xi) - \tanh\left(\frac{\xi}{2}\right), \\
T_3(\xi) &= \left(2\alpha^2 \tanh(\alpha\xi) \tanh\left(\frac{\xi}{2}\right) - \alpha\right) \tanh\left(\frac{\xi}{2}\right), \\
T_4(\xi) &= \left(2\alpha^2 \tanh\left(\frac{\xi}{2}\right) - \alpha \tanh(\alpha\xi)\right) \tanh\left(\frac{\xi}{2}\right), \\
T_5(\xi) &= 2\alpha + \tanh\left(\frac{\xi}{2}\right), \qquad T_6(\xi) = 2\alpha - \tanh\left(\frac{\xi}{2}\right), \\
T_7(\xi) &= \left(\alpha + 2\alpha^2 \tanh\left(\frac{\xi}{2}\right)\right) \tanh\left(\frac{\xi}{2}\right), \quad T_8(\xi) = \left(\alpha - 2\alpha^2 \tanh\left(\frac{\xi}{2}\right)\right) \tanh\left(\frac{\xi}{2}\right).
\end{aligned}$$

Then the neutral curve relations can be given by

$$ST_5(d)T_8(d) - T_6(d)T_7(d) - J_0T_5(d)T_6(d) = 0 \quad \text{unconfined}, \tag{3.19}$$

$$T_1(h)\left[ST_4(d)T_5(d) + T_2(d)T_7(d)\right] + T_2(h)\left[ST_3(d)T_5(d) + T_1(d)T_7(d)\right] + J_0T_5(d)\left[T_1(d)T_2(h) + T_1(h)T_2(d)\right] = 0 \quad h_2 = h,\ h_1 = \infty \tag{3.20}$$

$$T_1(h)\left[ST_2(d)T_8(d) + T_4(d)T_6(d)\right] - T_2(h)\left[ST_1(d)T_8(d) + T_3(d)T_6(d)\right] + J_0T_6(d)\left[T_1(d)T_2(h) - T_1(h)T_2(d)\right] = 0 \quad h_1 = h,\ h_2 = \infty \tag{3.21}$$

$$\begin{aligned}(S-1)\left[T_1(h)^2T_2(d)T_4(d) - T_2(h)^2T_1(d)T_3(d)\right] \\ +(1+S)T_1(h)T_2(h)\left[T_2(d)T_3(d) - T_1(d)T_4(d)\right] \\ -J_0\left[T_1(h)^2T_2(d)^2 - T_1(d)^2T_2(h)^2\right] = 0 \quad h_{1,2} = h,\end{aligned} \tag{3.22}$$

$$\begin{aligned}(S-1)\left[T_1(h_1)T_1(h_2)T_2(d)T_4(d) - T_2(h_1)T_2(h_2)T_1(d)T_3(d)\right] \\ +T_2(d)T_3(d)\left[T_2(h_1)T_1(h_2) + ST_1(h_1)T_2(h_2)\right] \\ -T_1(d)T_4(d)\left[T_1(h_1)T_2(h_2) + ST_2(h_1)T_1(h_2)\right] \\ +J_0\left[T_1(h_1)T_2(d) - T_1(d)T_2(h_1)\right]\left[T_1(h_2)T_2(d) + T_1(d)T_2(h_2)\right] = 0 \quad h_1 \neq h_2.\end{aligned} \tag{3.23}$$

The unconfined condition (3.19) can be expanded and written as a cubic polynomial in α with coefficients depending on d, S and J_0

$$\begin{aligned}4(S+1)\tanh^2\left(\frac{d}{2}\right)\alpha^3 - 2\left[(S-1)\tanh\left(\frac{d}{2}\right)\operatorname{sech}^2\left(\frac{d}{2}\right) + 2J_0\right]\alpha^2 \\ -(S+1)\tanh^2\left(\frac{d}{2}\right) + J_0\tanh^2\left(\frac{d}{2}\right) = 0,\end{aligned}$$

that has a positive root, which for $J_0 = 0$ is

$$\alpha = \frac{(S-1)\operatorname{sech}^2\left(\frac{d}{2}\right) + \left[(S-1)^2\operatorname{sech}^4\left(\frac{d}{2}\right) + 4(S+1)^2\tanh^2\left(\frac{d}{2}\right)\right]^{1/2}}{4(S+1)\tanh\left(\frac{d}{2}\right)}. \tag{3.24}$$

This value is a constant for a given $d \neq 0$ and S and corresponds to the $h_{1,2} \to \infty$ limit of the other cases in (3.20)-(3.23). When $S = 1$ this reduces to $\alpha = 1/2$ and all the other relations reduce to the equivalent results from Healey (2009), as is shown in § B of the supplementary material.

The results considered here in (3.19)-(3.23) with $d \neq 0$ can be used to define the neutral curves, we plot examples of these neutral curves for $S = 5$, $d = 1$ with (a) $J_0 = 0$, $h_2 = 3h_1/2$, (b) $J_0 = 0$, $h_2 = 9h_1/10$ and (c) $J_0 = 0.3$, $h_2 = 3h_1/2$ can be found in figure 3. Here the flow is unstable under (and to the right of) the solid lines. As the curves lie progressively further to the right (larger values of h), then the flows become progressively more stable as we move in this direction. For example, in panel (a) the symmetrically confined result (result 3) is more stable than the two semi-confined results (results 1&2), but the asymmetric result with $h_2 = 3h_1/2$ (result 4) is more stable than this symmetric result. In panel (b) we have a case with $\delta < 0$ in (3.11) ($h_2 = 9h_1/10$) and in this case we showed analytically in §3.1 that the asymmetric case can be more unstable than the symmetric case, which is confirmed here, with the positions of results 3 and 4 reversed, although the neutral curves lie close to each other. In panels (a) and (b) the dotted line gives the result of the asymptotic result (3.16), while result 2 terminates at $h = 1$ because at this point the upper plate would meet the density interface, changing the problem to a homogeneous problem. In panel (c) we consider the same case as in (a) except with $J_0 = 0.3$. Here we find that the significant difference with the $J_0 = 0$ case is that each result

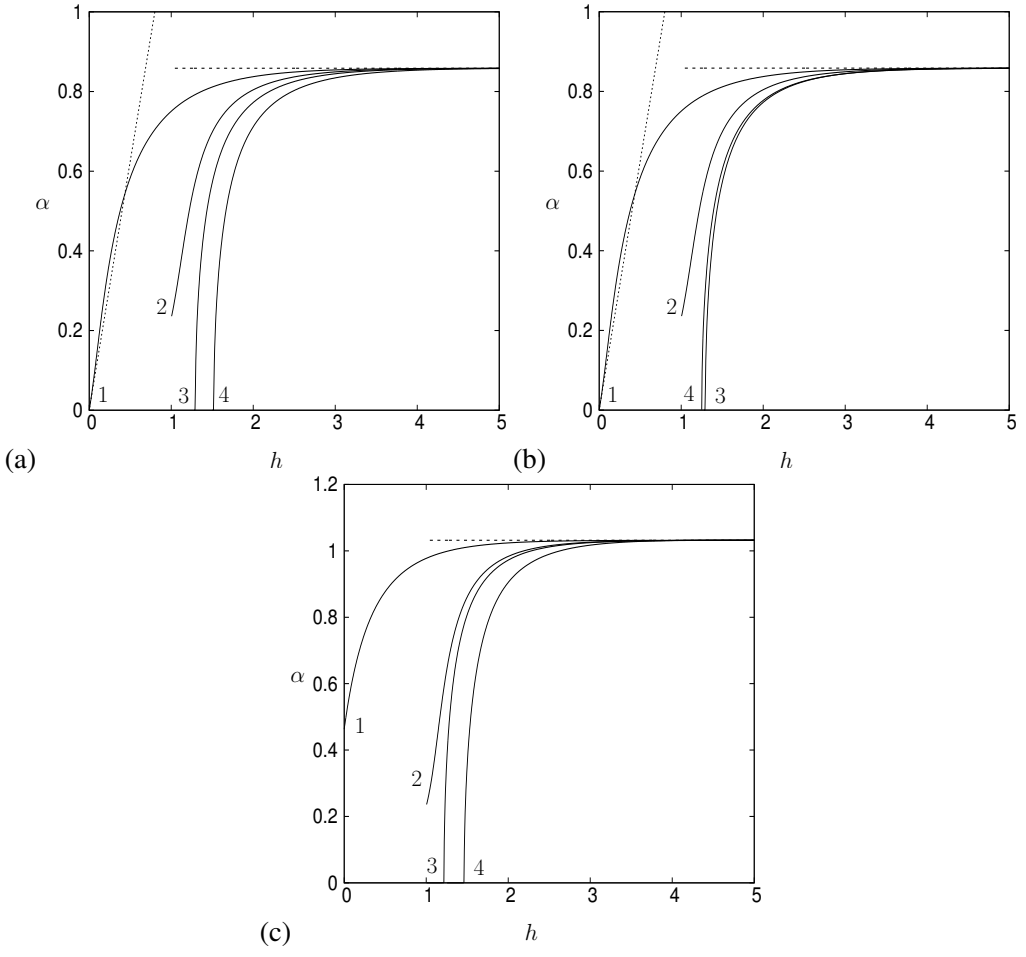

Figure 3. Plot of the temporal neutral curve of the KH modes for the cases $S = 5$, $d = 1$ with (a) $J_0 = 0$, $h_2 = 3h_1/2$, (b) $J_0 = 0$, $h_2 = 9h_1/10$ and (c) $J_0 = 0.3$, $h_2 = 3h_1/2$. The horizontal dashed line is the neutral curve for the unconfined shear layer (3.24), while the other results are neutral curves for 1- semi-confined shear layer with $h_2 = h$ (3.20), 2- semi-confined shear layer with $h_1 = h$ (3.21), 3- symmetrically confined shear layer with $h_1 = h_2 = h$ (3.22) and 4- asymmetrically confined shear layer with the above plate position ratios and $(h_1 + h_2)/2 = h$ (3.22). The dotted lines represent the small α asymptotic result (3.16) in (a) and (b). In each panel, result 2 terminates at $h = 1$ because this is the point at which the upper plate meets the density jump producing a homogenous shear layer.

is more unstable than the corresponding $J_0 = 0$ result, with unstable modes existing for a larger range of α values.

Figure 3 shows that for $h \geq 5$ the effect of confinement on the neutral curve for symmetric confinement is small, but the stabilizing effect on the growth rate $\mathrm{Im}(\omega) = \mathrm{Im}(\alpha c)$ for $h \leq 5$ is significant, see figure 4. These growth rates need to be calculated numerically by solving (2.9) directly for the (now) complex eigenvalue c, and unlike on the neutral curve, these results depend on the shear rate r, which we set to $r = 1$ here. These plots are essentially vertical slices through the results in figures 3(a) and 3(c).

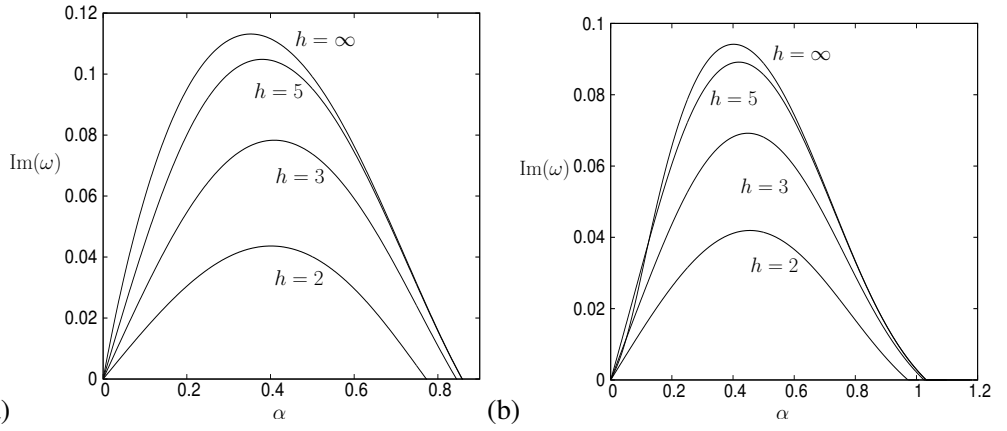

Figure 4. Temporal instability growth rates of the KH modes for the shear layer (2.14) with $r = 1$ for the cases given in (a) figure 3(a) and (b) figure 3(c), confined by symmetric plates at $y = \pm h$. The curve labeled $h = \infty$ corresponds to the unconfined result.

3.3. *Confinement effect on the tanh shear layer for internal modes*

Here we examine the internal modes which are unstable for $J_0 \neq 0$, and $J_0 = 0$ with $d \leq 0$. As discussed in relation to figure 2, the internal modes in these cases persist to large values of α, and in § C of the supplementary material we show that these modes are unstable for all α as $\alpha \to \infty$ (i.e. the short-wave limit) for the case $J_0 = 0$. Therefore, while all the results of §3.2 still hold, it becomes more difficult to define a neutral temporal stability curve as wavenumbers are unstable down to quite short waves.

The $J_0 = 0$ results in § C of the supplementary material, which will be perturbed a small amount for small $J_0 \neq 0$, show two key features. Firstly, the growth rate of these internal modes (for the density jump case), decay to zero like α^{-2} and so in a physical system one would expect these modes to ultimately stabilize due to small effects such as surface tension and viscosity. Secondly, the width of the eigenmode is $O(\alpha^{-1})$ about $y = d$, and so for $\alpha \gtrsim 4$ or so, the eigenmode stops feeling the effect of the confining plates and thus the neutral curve results for the symmetric and asymmetric confinement results become identical. Therefore, the effect of asymmetric confinement for both the KH and internal modes is most readily felt for long waves, which is consistent with the absolute instability results we present in this paper, and those which were found in Healey (2009) for the homogeneous case.

The results in this section have identified that the temporal stability of the stratified shear layer is predominately more unstable for the symmetrically confined scenario as opposed to the asymmetric confined case, except for a small region of parameter space. Our focus now is to determine how asymmetry of the system (both asymmetric confinement and $d \neq 0$) affects the absolute instability of these stratified shear flows.

4. Long-wavelength dispersion relations

Before we examine the absolute instability (AI) properties of these stratified shear flows, we first consider the long-wavelength disturbances for AI. When we consider disturbances with wavelengths longer than the thickness of the shear layer, then a suitable approximation for the velocity function (1.1) is to consider a step function where $f(y) = -1$ for $y < 0$ and $f(y) = 1$ for $y > 0$. This profile allows for an analytic form of the dispersion relation to be derived, which is fast and straight forward to solve numerically. This is helpful for

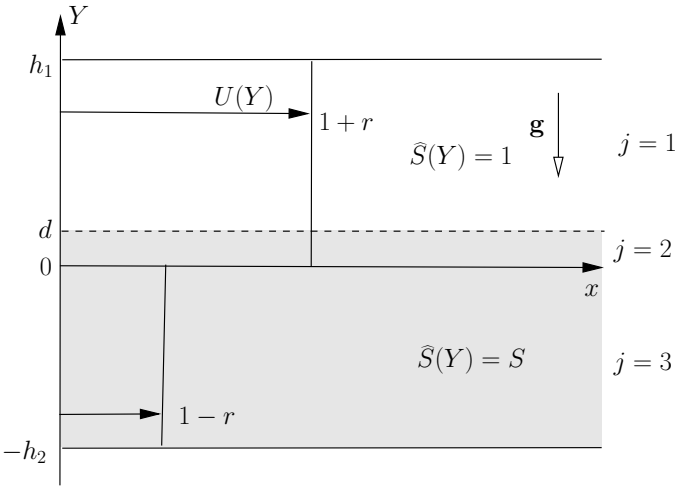

Figure 5. Schematic of the piecewise-linear, long-wave form of the problem for the case $d > 0$ and $r > 0$.

plotting contours of ω in the complex α-plane, which is an essential part of identifying the existence of pinch point saddles, as described in §5. For the homogeneous shear layer, Healey (2009) identified that it is these long-wavelength disturbances which are significant to the form of the neutral stability curve, especially at stronger confinements. The same observation was also made by Juniper (2006) for confined jets and wakes. In anticipation that long-wave solutions will be significant in the confinement of asymmetric stratified shear flows, we construct the long-wavelength dispersion relations here.

If we let $0 < \epsilon \ll 1$ be a small parameter which characterizes the size of the wavenumber, then if the plate separation is of $O(\epsilon^{-1})$, i.e. of order of the wavelength of the disturbance, and we let the position of the density jump also be $O(\epsilon^{-1})$ away from the shear layer, then both these effects enter the problem at leading order. Healey (2009) showed that the scaling on the phase speed $c = \omega/\alpha$ is the same as for the Kelvin-Helmholtz instability, namely

$$\alpha = \epsilon\alpha_0, \qquad \omega = \epsilon c_0\alpha_0 + O(\epsilon^2), \tag{4.1}$$

with the boundary conditions

$$v(h_1/\epsilon) = 0, \quad v(-h_2/\epsilon) = 0,$$

and with the density jump at $y = d/\epsilon$. Healey (2009) also showed that $v = O(\epsilon)$ in these regions.

Inside the shear layer and the density jump layer the variable $y = O(1)$ but outside these layers we introduce a slow spatial variable $Y = \epsilon y$, where $Y = O(1)$. Therefore the shear and density layers are significantly thinner than the rest of the flow domain, and so the consequence of this is, we can determine the long-wave dispersion relations by solving the piecewise-linear form of the problem, as depicted in figure 5, for the case $r > 0$ and $d > 0$. Here, in the three layers, the base flow velocity and density profiles are constants, and so the solutions satisfy

$$\frac{\mathrm{d}^2 v_j}{\mathrm{d}Y^2} - \alpha_0^2 v_j = 0, \tag{4.2}$$

to be solved with the jump conditions (2.13), which now need to be solved at $Y = 0$ as well as $Y = d$.

For the case in figure 5 we solve (4.2) in each layer with the respective boundary conditions at $Y = h_1,\ -h_2$ to give

$$v_1 = A\sinh\alpha_0(Y - h_1), \tag{4.3}$$
$$v_2 = B\cosh\alpha_0 Y + C\sinh\alpha_0 Y, \tag{4.4}$$
$$v_3 = D\sinh\alpha_0(Y + h_2). \tag{4.5}$$

Matching at $Y = 0$ and $Y = d$ leads to

$$B = \frac{1 + r - c_0}{1 - r - c_0} D\sinh\alpha_0 h_2, \tag{4.6}$$
$$C = \frac{1 - r - c_0}{1 + r - c_0} D\cosh\alpha_0 h_2, \tag{4.7}$$
$$A\sinh\alpha_0(d - h_1) = B\cosh\alpha_0 d + C\sinh\alpha_0 d, \tag{4.8}$$
$$A\cosh\alpha_0(d - h_1) - S\left[B\sinh\alpha_0 d + C\cosh\alpha_0 d\right] = \frac{(1 - S)F^{-2}}{\alpha_0(1 + r - c_0)^2} A\sinh\alpha_0(d - h_1). \tag{4.9}$$

The dispersion relation for $d > 0$ is then found via a non-trivial solution to this system of equations. The full set of long-wave dispersion relations used for both finite and infinite h_1 and h_2 can be found in § D of the supplementary material.

5. Absolute instability of symmetrically confined shear layers

To determine the absolute instability (AI) properties of a flow we consider a spatio-temporal stability analysis where both α and ω are allowed to be complex. We are interested in seeking whether instability wavepackets have growth, $\mathrm{Im}(\omega) = \omega_i > 0$, along the characteristic

$$\frac{x}{t} = 0,$$

i.e, at the point at which the instability disturbance is generated. Spatio-temporal theory has been documented in many works such as Briggs (1964), Huerre & Monkewitz (1990), Healey (2006*a*, 2007), Juniper (2006, 2007), Garrett & Peake (2007), Brambley (2010), Pier & Peake (2015) and Poole & Turner (2023, 2024) to name a few, and the reader is directed to these works and references therein for more information. Determining the AI characteristics of the flow can be shown to amount to seeking the value of ω_i at special saddle points of contours of ω_i in the complex α-plane. These special saddle points are known as *pinch points*, and can be determined via the Briggs criterion (Briggs 1964), which effectively states that the Fourier inversion contour, which runs along the real α-axis, can be deformed onto the saddle, while remaining in the valleys of the saddle in the rest frame (Healey 2006*b*). For the results which follow in §5 and §6.1 we check whether our saddle points are pinch points in the following two ways: firstly we plot contours of ω_i = constant, such as those in figure 6, for various confinement and asymmetry parameters and determine by eye whether the Fourier inversion contour can be deformed off the real α-axis and through the saddle, while remaining in the valleys of the saddle; secondly, in ambiguous cases where a pinch point cannot be determined by eye, we explicitly use Briggs criterion to determine whether the saddle is one which pinches upstream and downstream propagating branches of solutions.

For a given set of parameters h_1, h_2, S, d, r, we find the 4 unknowns $\alpha_r, \alpha_i, \omega_r$ and ω_i (where $\alpha = \alpha_r + \mathrm{i}\alpha_i$, $\omega = \omega_r + \mathrm{i}\omega_i$) by solving

$$\mathbb{D}(\alpha, \omega) = \frac{\partial \mathbb{D}}{\partial \alpha}(\alpha, \omega) = 0, \tag{5.1}$$

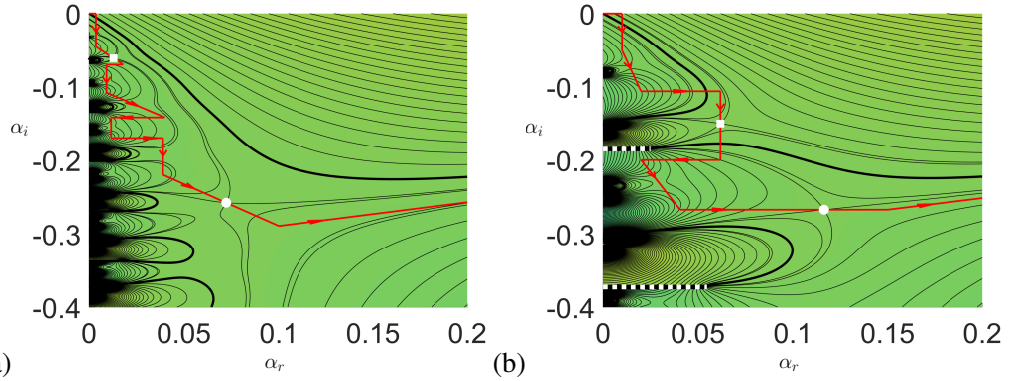

Figure 6. Plot of ω_i contours in the α-plane for $S = 2$, $r = 1.09$, $d = F^{-2} = 0$ for symmetric confinement with (a) $h = 50$ and (b) $h = 20$. The white circle and square denote the dominant pinch points in the case $h = 50$ and $h = 20$ respectively, the thick black contour signifies the value $\omega_i = 0$, the black and white lines denote branch cuts and the red contour signifies an example path for the Fourier inversion contour. In (a) the flow is convectively unstable with $\omega_i = -0.00451$ (circle saddle) and in (b) the flow is absolutely unstable with $\omega_i = 0.00579$ (square saddle).

simultaneously using Newton's method. From an initial guess (α^0, ω^0) the n^{th} iterate of (α^n, ω^n) is updated via

$$\begin{pmatrix} \alpha^{n+1} \\ \omega^{n+1} \end{pmatrix} = \begin{pmatrix} \alpha^n \\ \omega^n \end{pmatrix} - \begin{pmatrix} \mathbb{D}_\alpha(\alpha^n, \omega^n) & \mathbb{D}_\omega(\alpha^n, \omega^n) \\ \mathbb{D}_{\alpha\alpha}(\alpha^n, \omega^n) & \mathbb{D}_{\alpha\omega}(\alpha^n, \omega^n) \end{pmatrix}^{-1} \begin{pmatrix} \mathbb{D}(\alpha^n, \omega^n) \\ \mathbb{D}_\alpha(\alpha^n, \omega^n) \end{pmatrix},$$

where the subscripts denote partial derivatives. We continue iterations until $||(\alpha^{n+1}, \omega^{n+1}) - (\alpha^n, \omega^n)||_2 < 10^{-8}$, at which point we consider the solution to be converged.

Our main interest is in determining the position of the neutral stability curve for a given set of system parameters, and so in this case our vector of unknowns is $(\alpha_r, \alpha_i, \omega_r, r)^T$, as $\omega_i = 0$ on this curve. We again find these values using Newton's method, but this time we split the two complex equations in (5.1) into four real equations for numerical convenience.

Despite our interest being on how asymmetry of the system affects the AI properties, we begin first by considering a symmetrically confined shear layer with $h_1 = h_2 = h$, and in particular with $d = 0$. In this case we are restricted to numerical solutions of the full system only, because the long-wavelength theory in (D-1) and (D-2) of the supplementary material both simplify to

$$\left[(c_0 + r - 1)^2 S + (c_0 - r - 1)^2\right] \tanh(\alpha_0 h) + (S - 1) F^{-2} \frac{\tanh^2(\alpha_0 h)}{\alpha_0} = 0.$$

When $F^{-2} = 0$, this has no dispersive terms, i.e. no saddle points and thus no AI properties of the shear layer. In this case the long-wave theory breaks down as dispersion is a higher order effect. However, when $d \neq 0$ the long-wave theory does not breakdown for symmetric confinement, as we will see later, and dispersion returns as a leading order effect.

In figure 6 we consider the form of the ω_i = constant contours for the cases $S = 2$, $r = 1.09$, $d = F^{-2} = 0$ with (a) $h = 50$ and (b) $h = 20$. In (a) the flow is convectively unstable, as the dominant pinch point saddle at $\alpha = 0.0723 - 0.2578\text{i}$ has $\omega_i = -0.00451$. The saddle at $\alpha = 0.0129 - 0.0609\text{i}$, also lies on the Fourier inversion contour (an example of this contour is denoted by the red contour in each panel), but has $\omega_i = -0.00934$ and so is sub-dominant to the other saddle. In this case, determining whether saddle points lie on the Fourier inversion contour is a straight forward task by eye, by determining how the

Fourier inversion contour is deformed off the α_r-axis while remaining in the valleys of the saddle points. The red inversion contour example for $h = 50$, comes along the α_r-axis from $\alpha_r = -\infty$ (not shown), and then passes down the left-hand side of the figure, passing through the string of saddles at $0.0036 - 0.0298\mathrm{i}$, $0.0129 - 0.0609\mathrm{i}$, $0.0092 - 0.0917\mathrm{i}$, $0.0254 - 0.1258\mathrm{i}$, $0.0116 - 0.1548\mathrm{i}$ and $0.0390 - 0.1924\mathrm{i}$ before finally passing through the saddle point at $0.0723 - 0.2578\mathrm{i}$ and back up to the α_r axis where it extends to $\alpha_r = \infty$. The dominant saddle in this case is the same saddle point which exists in the unconfined ($h \to \infty$) limit and so would determine the AI properties of the flow if the plates were not present. This *unconfined saddle* usually occurs with $\alpha_r = O(1)$, and thus is not determined by the long-wave theory. The array of saddles close to the imaginary axis are due to the inclusion of the bounding plates, which puts infinitely many poles along the imaginary axis at $\alpha = \alpha_p$ where α_p satisfies

$$S\tanh(\alpha_p(d-h)) - \tanh(\alpha_p(d+h)) = 0, \tag{5.2}$$

see § E of the supplementary material. When $S = 1$ or $d = 0$ this reduces to

$$\alpha_p = \pm\frac{n\pi}{2h}\mathrm{i},$$

as found in Healey (2009) for the homogeneous case. These poles, where $\omega_i \to -\infty$ are the points at which the inversion contour changes its value of ω_r, due to the negligible contribution to the inversion integral.

As the flow is further confined to $h = 20$ in figure 6(b), the saddle points move in the complex α-plane and we find scenarios where the confinement saddles dominate over the unconfined saddle. In this case the flow is absolutely unstable as the pinch point saddle at $\alpha = 0.0619 - 0.1502\mathrm{i}$ has the largest ω_i value with $\omega_i = 0.00579$. Note, in both panels of figure 6 the inversion contour eventually returns to the real α-axis at large values of α_r.

In figures 7(a,b) we consider the neutral AI curves for the symmetrically confined shear layer with $F^{-2} = d = 0$. The flows are absolutely unstable above the contours and convectively unstable below, and results with $r < 0$ are given by the dashed lines while $r > 0$ results are given by the solid lines. For the case $S = 2$ with $r = 1.09$ depicted in figure 6, we see for large h, the neutral curve is approximately constant and this is because here the unconfined saddle is dominant and varying the plate position doesn't alter its stability properties significantly, while for $h \lesssim 29$ the confinement saddle switches to being the dominant saddle. Here we find that the neutral curve moves to a smaller value of $|r|$, giving an AI for a larger set of parameters, ultimately making the flow more absolutely unstable. This change in saddle dominance is signified by the gradient discontinuities of the neutral curve.

Figure 7(a) shows that for $r < 0$ (i.e. having the faster stream in the denser fluid) the unconfined saddle is dominant for a large range of h. Whereas for $r > 0$ (i.e. having the slower stream in the denser fluid) the confined saddles become dominant for increasing values of h. The reason for this is, when $r < 0$ the wavelength of the unconfined mode reduces (α_r increases) for increasing h, and thus it moves further from the confined modes in the complex α-plane. For $r > 0$ the wavelength increases and thus the saddle moves towards the imaginary axis, allowing the confinement modes to more readily dominate the AI properties of the flow. In fact for $S \geq 5$, only confinement saddles contribute to the neutral curve for $h \leq 250$ given here. These confinement saddles cause the neutral curve to lower and for $S \geq 5$, the flow has a region of AI with $0 < r < 1$ which signifies a co-flow shear layer. The minimum r value is $r = 0.9402$ which occurs at $S = 8.5778$, as shown in in figure 8.

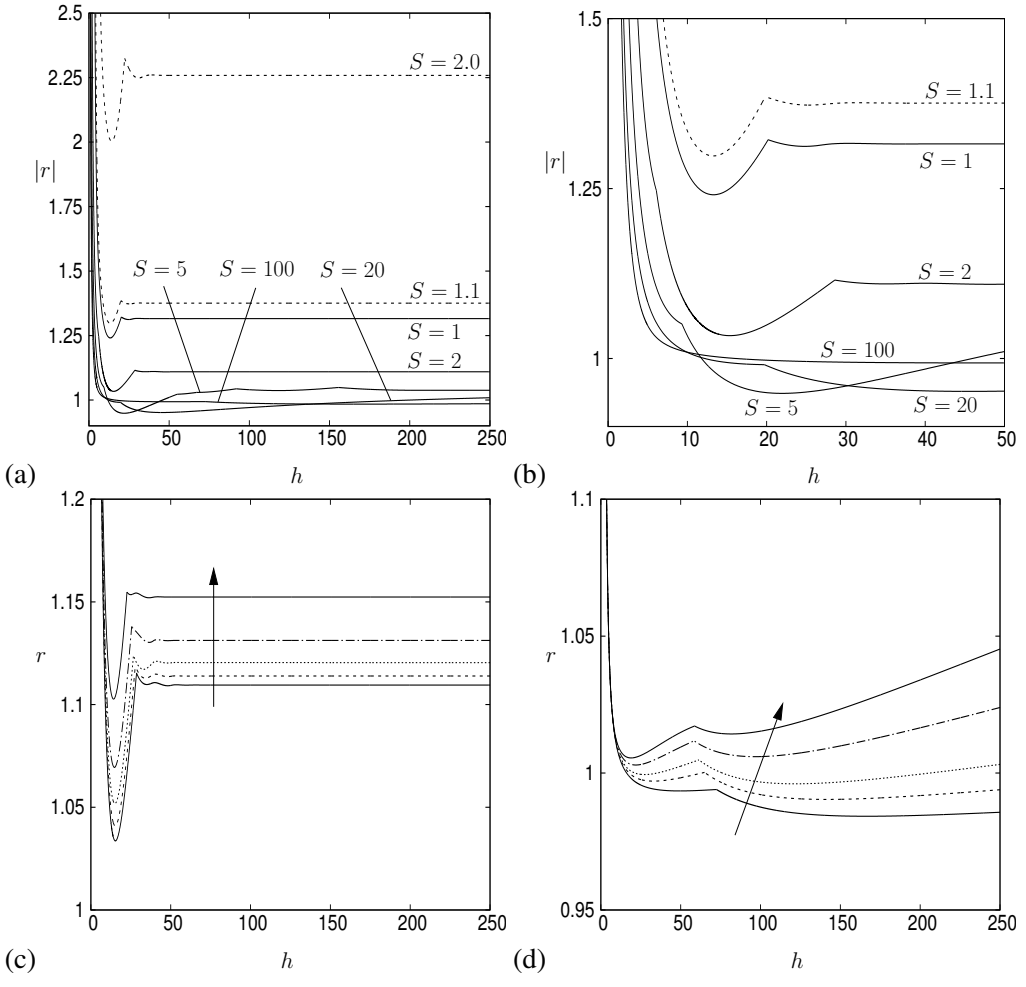

Figure 7. (a,b) Plot of the neutral curve for absolute instability for symmetric confinement in the (h, r)-plane for the case $d = F^{-2} = 0$ and $S = 1, 1.1, 2, 5, 20$ and 100. The solid lines represent cases with $r > 0$ and the dashed lines have $r < 0$. Above each neutral curve the flow is absolutely unstable and convectively unstable below. Panel (b) is a close-up of panel (a). In (c,d) we consider the cases $S = 2$ and $S = 100$ respectively with $d = 0$. The arrows show increasing Richardson numbers with $F^{-2} = 0.0, 0.01, 0.025, 0.05, 0.1$ in (c) and $F^{-2} = 0.0, 0.0001, 0.0002, 0.0004, 0.0006$ in (d).

In figures 7(c,d) we consider the neutral curves for the cases $S = 5$ and $S = 100$ respectively when the Richardson number and hence $F^{-2} \neq 0$. In this work our focus is on high-speed flows, i.e. small Richardson numbers or large Froude numbers, such that the results are a small perturbation from the $F^{-2} = 0$ results, but here we consider a range of F^{-2} values such that its effect on the results can be observed. The results in figures 7(c,d) show that increasing F^{-2} has the effect of stabilizing the AI of the flow, i.e. raising the neutral curves, but the effect of the confining modes dominating the AI properties for small and moderate confinements is still evident.

In this symmetrically confined scenario we now consider how the neutral stability region is affected by moving the mean density position, d, away from $y = 0$ in figure 9 for the case $F^{-2} = 0$ with $r > 0$. Here the solid line gives the neutral curve of the shear flow in the $(r, d/h)$-plane with $h = 100$ fixed, and the dashed line represents the neutral curve of

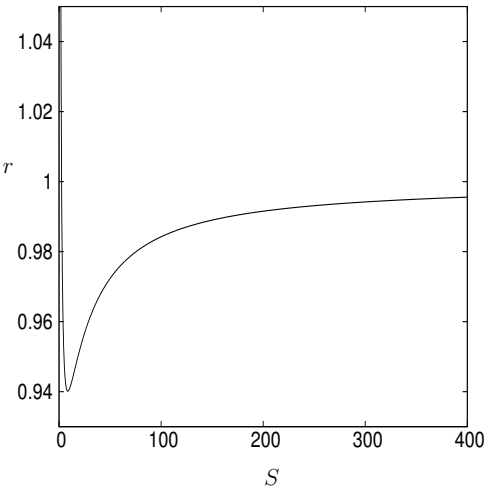

Figure 8. Plot of the minimum r value as a function of S for the symmetric confinement neutral curves in figure 7(a,b) for $F^{-2} = 0$ and $r > 0$.

the long-wave dispersion relation from §4. All the results show genuine asymmetry, with the minimum value of $r > 0$ occurring for $d < 0$ in each case. For $S = 2$, the value of $h = 100$ is such that for $d = 0$, the confined saddles do not determine the flow stability properties and so as d is varied, the long-wavelength result greatly differs from the actual calculated result. The result also very quickly tends to a constant r for $|d/h| \gtrsim 0.2$ which is just the result for a tanh shear layer in a single fluid, i.e. the effect of the second fluid stream not containing the shear layer has become less significant to the calculation. For the results $S = 5$ and 20, the confinement saddles become more significant and we see a range of d/h values where the long-wave results agree well with the actual results. This occurs more predominantly for $d > 0$ where the centre of the shear layer lies in the denser of the two fluids. For $S = 100$ in panel (d) the results again have a minimum r for $d/h < 0$, but in this case there appears to be a mode for which the flow is unstable with $r = 1$ for $d/h < 0$. However, this is a mode for which $\alpha_r \to 0$ at this neutral value. Juniper (2006) argues that these modes should be discounted on the physical grounds that these modes have large wavelength, violating the fixed base flow assumption, and as they decay slowly in the y-direction, their amplitude should tend to zero to avoid having infinite energy. Applying this reasoning here, the small dotted line close to $d/h = 0$ plots the contour for modes which have $\alpha_r = 0$. The flow is then absolutely unstable for $(d/h, r)$ values above the upper solid line for $d/h < 0$, which agrees with the long-wave approximation for a range of values.

The key result from figure 9 is the existence of a shear rate value, r, smaller that that when $d = 0$, for which the flow is absolutely unstable, essentially showing density asymmetry can further destabilize the flow. In figure 10 we re-plot the neutral curves for (a) $S = 2$ and (b) $S = 20$ with $d = 0$ from figure 7 and compare the result to the curve with $d = d_{\min}$. The results show that varying d to $d_{\min}$ can have a sizable effect on the position of the neutral curve, even producing a region of co-flow for $S = 2$ which is not present when $d = 0$. The discontinuities in the neutral curve occur at the points where the saddles switch dominance, but these discontinuities would not be observed in an experiment by varying the confinement parameter only, because the value $d_{\min}$ also varies along these curves. For a fixed value of d the neutral curve would be continuous, but could still lie below the $d = 0$ result at specific h values.

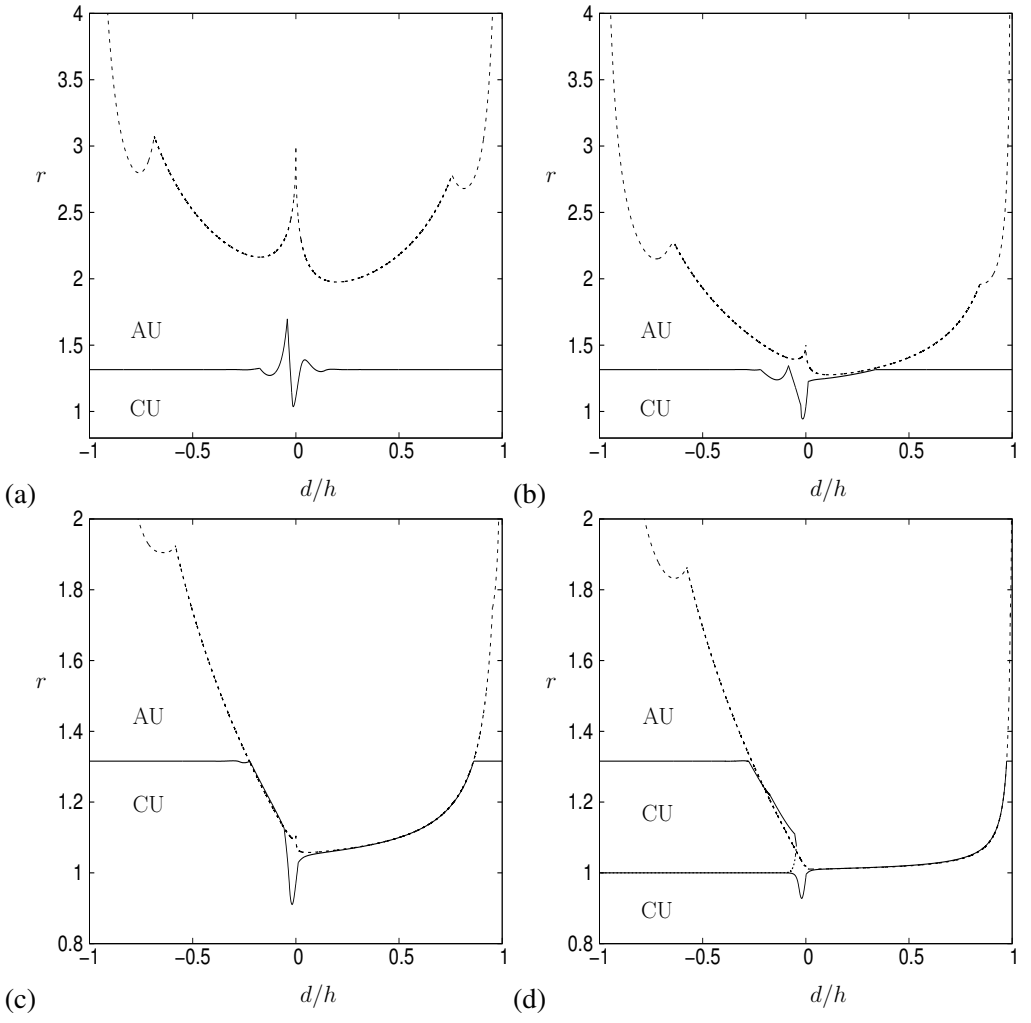

Figure 9. Plot of the neutral curve for absolute instability in the $(d/h, r)$-plane for the cases (a) $S = 2$, (b) $S = 5$, (c) $S = 20$ and (d) $S = 100$ for symmetrically confined flow with $F^{-2} = 0$. The solid lines represent the neutral curve for the full problem, while the dashed lines represent the results from the long-wave analysis. In (d) the dotted line for $d/h < 0$ represents the contour where $\alpha_r = 0$. At this point the contribution from this saddle should be discounted (Juniper 2006). Here AU and CU denote regions which are absolutely and convectively unstable respectively.

In figure 11(a,b) we consider the $S = 2$ and $S = 20$ cases from figure 9 except with $F^{-2} \neq 0$. As we saw in figure 7, increasing F^{-2} acts to stabilize the AI by raising the neutral curves. In figure 11(a) there is a small region of $d < 0$, around $r \approx 1.6$, where the neutral curve is lowered, but overall, the effect of including gravity effects appears to act to smooth out the neutral curve to that value of r at large values of $|d/h|$. Increasing F^{-2} also has the effect of moving the $d_{\min}$ value towards $d = 0$, and hence in an experimental flow scenario, this destabilization effect maybe harder to observe.

Having established that moving the mean density position away from the centre of the shear layer destabilizes the flow, we next investigate the effect of asymmetric confinement.

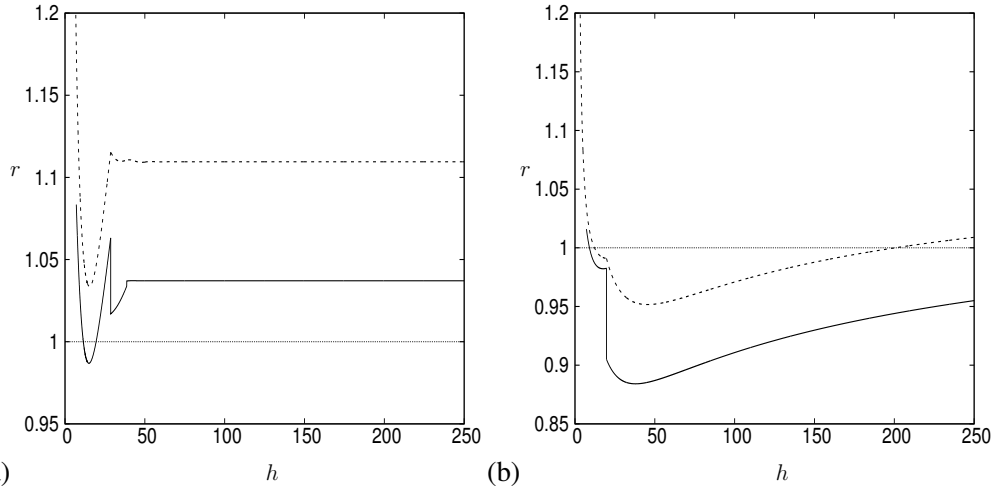

Figure 10. Plot of the neutral curve for absolute instability in the (h, r)-plane for the cases (a) $S = 2$ and (b) $S = 20$ with $F^{-2} = 0$ for a symmetrically confined flow. In each panel the dashed line is the $d = 0$ result from figure 7, while the solid lines give the equivalent neutral curve with $d = d_{\min}$. Above the neutral curve the flow is absolutely unstable and convectively unstable below.

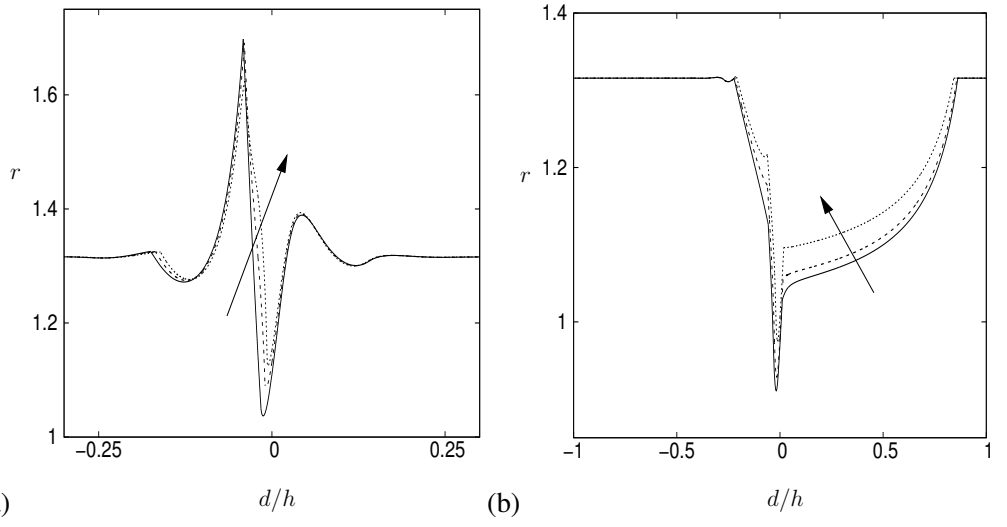

Figure 11. Plot of the neutral curve for absolute instability in the $(d/h, r)$-plane for the cases (a) $S = 2$, (b) $S = 20$ for symmetrically confined flow with $F^{-2} \neq 0$. In each case the arrows show results with increasing F^{-2} with $F^{-2} = 0.0, 0.05, 0.1$ in (a) and $F^{-2} = 0.0, 0.0005, 0.002$ in (b).

6. Absolute instability of asymmetrically confined shear layers

6.1. *Finite asymmetric confinement*

In this section our focus is on the effect of asymmetric confinement of the stratified shear layer, so we fix $d = 0$ such that the centre of the shear layer and the mean density position coincide. In this section we also only consider the limiting case when $F^{-2} = 0$. We have seen that the effect of $0 < F^{-2} \ll 1$ in §5 acted to stabilize the AI by raising the value of r on the neutral curve, while retaining the qualitative features of the $F^{-2} = 0$ result. Here we assume the same qualitative effect of having $F^{-2} \neq 0$ will be observed and hence why

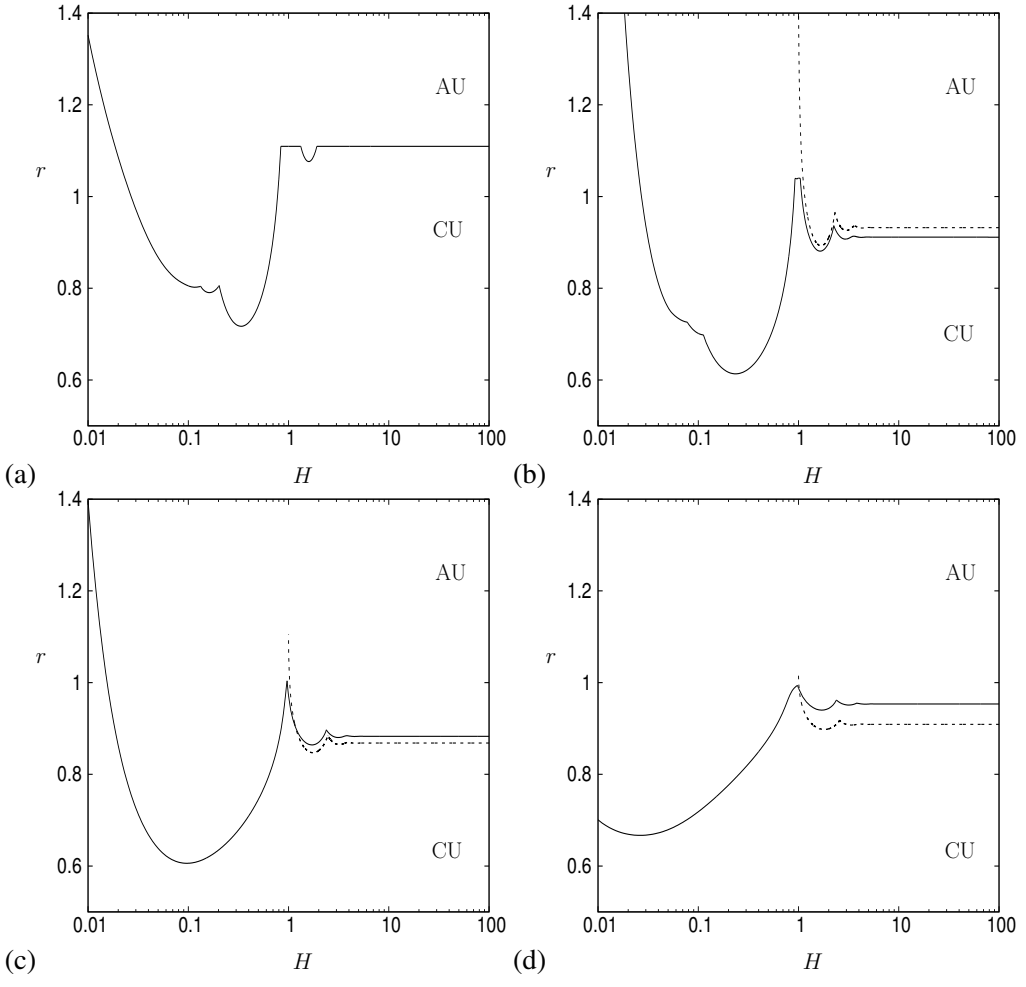

Figure 12. Plot of the neutral curve for AI in the (H, r)-plane for the case (a) $S = 2$, (b) $S = 5$, (c) $S = 20$ and (d) $S = 100$. The solid lines represent the neutral curve for the full problem, while the dashed lines represent the results from the long-wave analysis. Here the flow is asymmetrically confined with $h_2 = 100$ and $h_1 = Hh_2$ with $d = F^{-2} = 0$.

we only consider the $F^{-2} = 0$ case. We will however, reconsider the $F^{-2} \neq 0$ effect when we consider a continuous density profile in §7. In figure 12 we examine a fixed lower plate at $h_2 = 100$ and a variable upper plate with $h_1 = Hh_2$, where the asymmetry parameter H is varied to trace out the neutral curve in the (H, r)-plane. Here we only consider $r > 0$ as these cases see the largest effect due to the confined modes. These results show that asymmetric confinement with $H < 1$ and $H > 1$ both produce a destabilizing effect on the flow away from the symmetric case ($H = 1$). The most dramatic effect occurs for $H < 1$ which is the case when the less dense side of the shear layer is more strongly confined. The minimum values of $r_{\min} = r(H_{\min})$ and the corresponding $H_{\min}$ values are given in table 1. We observe that the value of $H_{\min}$ reduces with increasing S, while $r_{\min}$ has a minimum in $5 \leq S \leq 100$. For $H > 1$ we plot the results from the long-wave theory as the dashed lines for $S \geq 5$, and these show good qualitative agreement with the general results. For $S = 2$ in panel (a) the long-wave theory is not a good approximation to the general result because as $H \to \infty$ the dominant saddle is the unconfined saddle, not a saddle related to confinement,

	h_1 Fixed		h_2 Fixed	
	$r_{\min}$	$H_{\min}$	$r_{\min}$	$H_{\min}$
$S = 1$	0.978	0.40	0.978	2.53
$S = 2$	0.717	0.34	0.716	3.00
$S = 5$	0.613	0.24	0.599	4.45
$S = 20$	0.606	0.10	0.564	13.05
$S = 100$	0.667	0.03	0.561	62.50

Table 1. Table of values of $r_{\min} = r(H_{\min})$ together with the corresponding $H_{\min}$ value for the neutral curves in figures 12 and 13, with $d = F^{-2} = 0$.

and so we don't add this result to the panel. This can be observed in the semi-confined results in §6.2. The reason for this increase in AI and the multiple minima of the neutral curve has been put down to the constructive interference of modes on either side of the shear layer having similar cross-stream wavelengths (Juniper 2006; Healey 2009).

In figure 13 we consider asymmetric confinement again, but here $h_1 = 100$ is fixed and $h_2 = Hh_1$ is varied. The results are similar to those seen in figure 12, with $r_{\min}$ again occurring when the more dense fluid domain is largest ($H > 1$ in this case). This time the long-wave theory is in good agreement for all S values, and for $S = 20$ and 100 the semi-confined limit result is given by the horizontal dotted line, which clearly has not been reached by the time $H = 100$. In (c) for $H > 30$ there is a frequent changing of the dominant saddle as the large H limit is reached. A similar observation was seen for jets and wakes in Juniper (2006) (see their figure 15, $S = 0.316$ and $S = 3.16$). This saddle switching occurs when there are a large number of confinement saddles with similar values of ω_i, closely situated next to the imaginary axis. Then as H increases the dominant saddle rapidly changes to one higher up the axis. It is worth noting that the asymmetrically confined shear layer in the long-wave limit has the same dispersion relation as a symmetrically confined jet/wake flow, and as a consequence, the results presented in figures 12 and 13 are related to figures 11 and 15 in Juniper (2006).

Where there is agreement, the long-wave theory gives excellent agreement with the full theory for $H > 1$, except near $H = 1$ where the long-wave theory breaks down with $d = 0$ as noted earlier. The robustness of the long-wave theory is investigated in § F of the supplementary material. With this robustness in mind, we use the long-wave theory to examine the qualitative behaviour of the minimum shear value $r_{\min}$ of the problem when we allow $d \neq 0$ in the asymmetrically confined case for $S = 20$ in figure 13. Here figure 14 shows that for asymmetric confinements with $H > 1$, the $d = 0$ result appears to be the most unstable case. For the four non-zero values of d considered, the neutral curve lies above the $d = 0$ neutral curve close to $H_{\min}$. A numerical verification of $d \in [-5, 5]$ confirms that the $d = 0$ case is most unstable scenario.

The conclusion of the results in this section and the previous section are that for near symmetric cases, $|H - 1| \ll 1$, moving the mean density position such that $d < 0$ makes the flow more unstable (i.e. reduces the value of r on the neutral curve), while for larger values of H the dominant saddle point passes to a *confinement saddle* and here asymmetric confinement dominates the AI properties of the flow and thus the $d = 0$ result is the most unstable result. For the $S = 20$ case in figure 13(c) this switching from a $d = 0$ saddle to a confinement saddle occurs at $H = 1.033$, hence there is only a small region of parameter

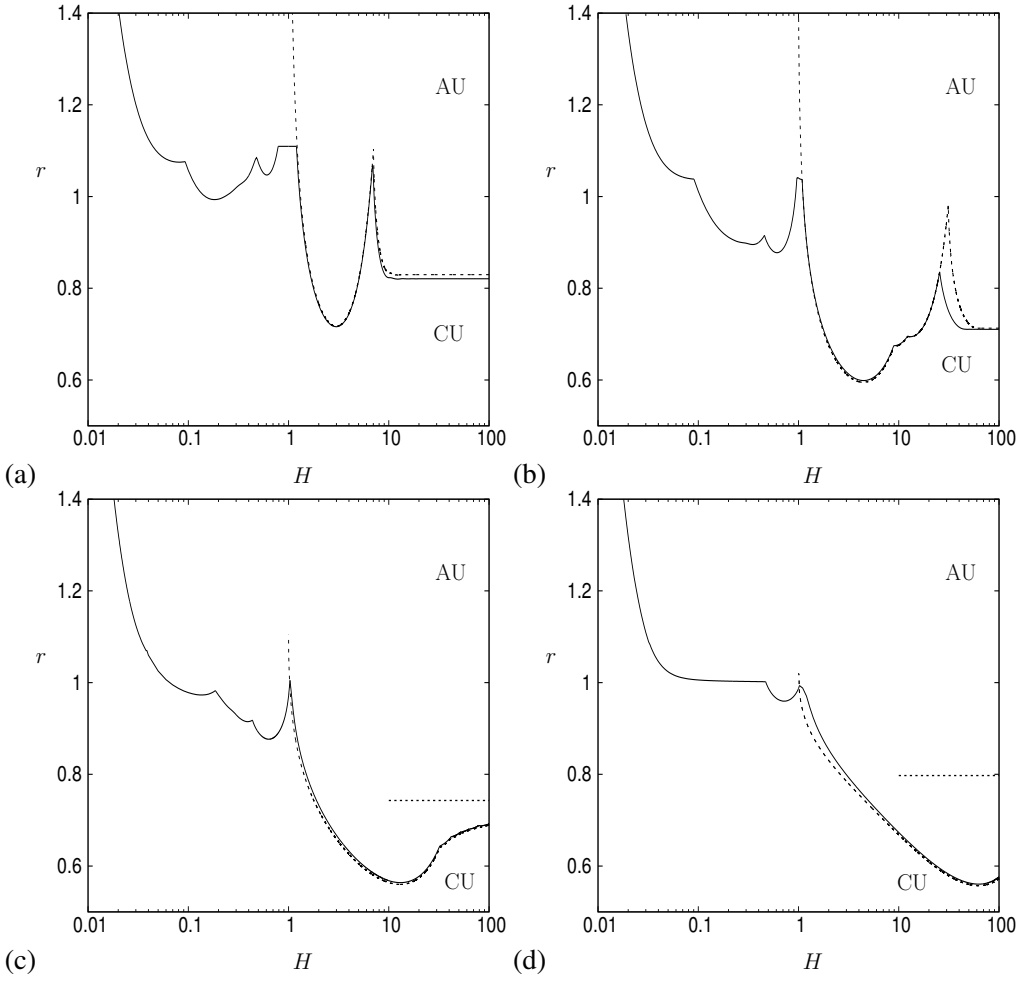

Figure 13. Plot of the neutral curve for AI in the (H, r)-plane for the case (a) $S = 2$, (b) $S = 5$, (c) $S = 20$ and (d) $S = 100$. The solid lines represent the neutral curve for the full problem, while the dashed lines represent the results from the long-wave analysis. Here the flow is asymmetrically confined with $h_1 = 100$ and $h_2 = Hh_1$ with $d = F^{-2} = 0$. The horizontal dotted lines in (c) and (d) give the corresponding semi-confined result.

space where having $d \neq 0$ is the dominant asymmetrical flow feature, but its effect can still be significant.

6.2. *Semi-confined shear layers (infinite asymmetric confinement)*

When the flow is confined by a single plate ($h_1 \to \infty$ or $h_2 \to \infty$), this is a form of asymmetric confinement which we call *semi-confinement*. In these cases, (2.9) and the jump conditions (2.13) are solved with one boundary condition from (2.10) and one from (2.11). For the homogeneous shear layer ($S = 1$) Healey (2009) showed that placing the plate in the faster stream of the shear layer enhanced the AI, while having the plate in the slower stream stabilized the AI.

For the stratified case, our findings show a more complicated situation. In figure 15 we consider the neutral curve in the $(h_{1,2}, r)$-plane for various density ratios for (a) $h_1 \to \infty$ and (b) $h_2 \to \infty$. The interpretation of these results is given in the schematic diagram in figure 16. This figure shows the four different scenarios under consideration, and the

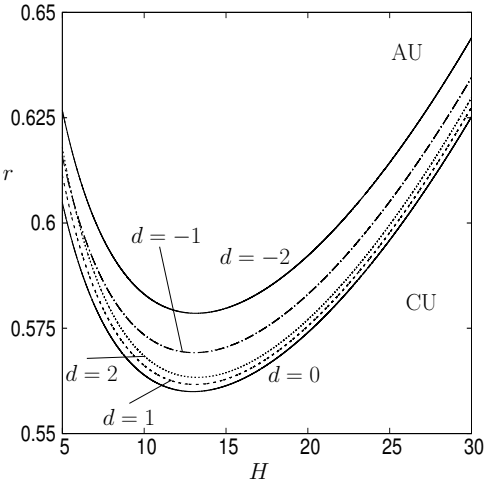

Figure 14. Plot of the neutral curve for the asymmetrically confined tanh shear layer in the (H, r)-plane close to the value $H_{\min}$ for $h_1 = 100$, $h_2 = Hh_1$, $S = 20$ in figure 13 and $d = 0, 1, 2, -1, -2$, with $F^{-2} = 0$.

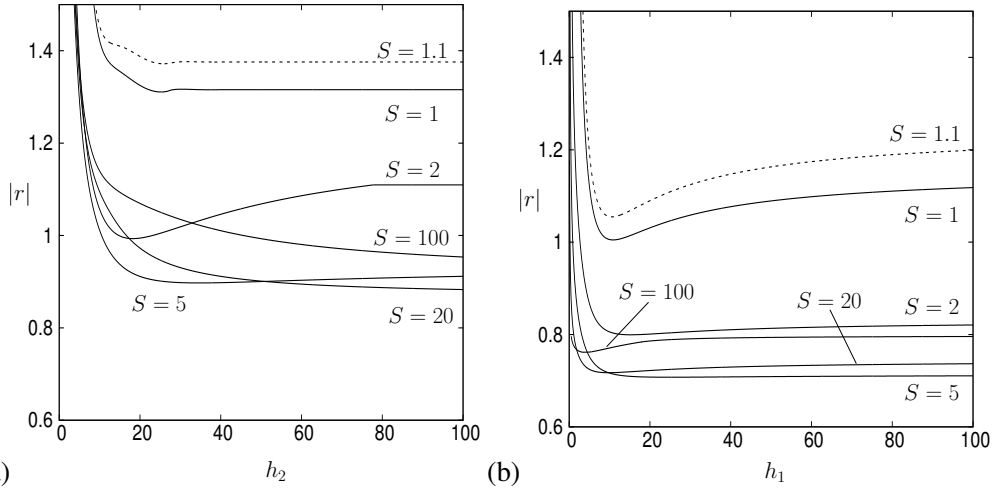

Figure 15. Plot of the neutral curves of the tanh shear layer for $S = 0.9, 1, 2, 5, 20, 100$ for the semi-confined shear flows for (a) the unconfined above case ($h_1 \to \infty$) and (b) the unconfined below case ($h_2 \to \infty$) with $d = F^{-2} = 0$. The solid lines represent cases with $r > 0$ and the dashed lines have $r < 0$.

directional arrows signify *is more unstable than*. We find that placing the plate in the faster and lighter stream is the most unstable configuration, while placing the plate in the slower and lighter stream is the least unstable configuration. The solid directional arrows signify that the second case is always more unstable than the first case, whereas the dashed arrow indicates that this second case is usually more unstable, but not for density ratios close to $S = 1$. This can be seen from the results in figure 15, because as S is increased from $S = 1$ with $r < 0$ in panel (b) and S is increased from $S = 1$ with $r > 0$ in panel (a), the results in (b) are more unstable initially (S close to 1), but ultimately the results in (a) are more unstable as S is increased further.

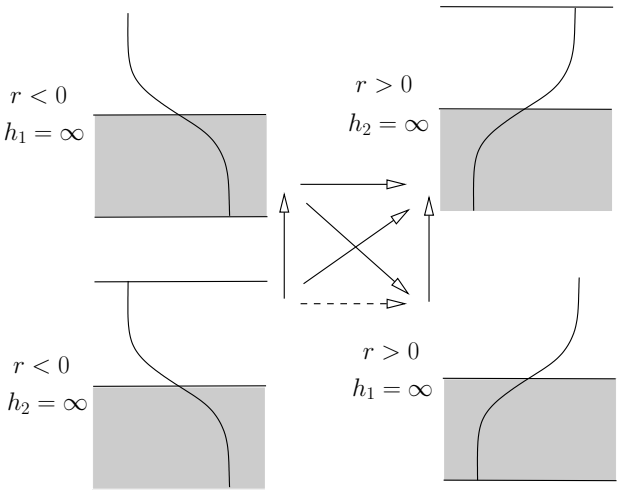

Figure 16. Schematic diagram of the 4 semi-confined scenarios considered in this paper. The directional arrow indicate *is more unstable than* with the solid arrows meaning the second flow is always more unstable than the first flow, while the dashed arrow means is usually more unstable than, except near $S = 1$.

6.3. *Stability hierarchy mechanism*

The semi-confinement hierarchy of results presented in figures 15 and 16 can be inferred from a simple model for the tanh shear layer, in a similar, but subtly different, argument to that presented in Healey (2009) for the homogeneous case. Here we consider the piecewise linear shear layer used by Rayleigh (1896)

$$f(y) = \begin{cases} 1 & \text{for} \quad y > 1 \\ y & \text{for} \quad -1 < y < 1 \\ -1 & \text{for} \quad y < 1 \end{cases} \tag{6.1}$$

together with the density profile (2.12). Substituting this into (2.9) and using the jump conditions (2.13), with $F^{-2} = 0$, one can derive the dispersion relation for the unconfined problem using the piecewise-linear approach as in §4 (Drazin & Reid 1981; Drazin 2002). The unconfined dispersion relation is given by the cubic polynomial in the phase speed $c - 1$,

$$(1+S)(c-1)^3 + \frac{r}{\alpha}(1-S)\left[1-e^{-2\alpha}\right](c-1)^2 - \frac{r^2}{\alpha^2}(1+S)\left[(2\alpha-1)^2 - e^{-4\alpha}\right](c-1)$$
$$+\frac{r^3}{\alpha^3}(S-1)\left[(2\alpha-1)+e^{-2\alpha}\right]^2 = 0,$$

whose solutions in the long-wave (small α) limit are

$$\begin{aligned} c_1 &= 1 + r\frac{S-1+\mathrm{i}\sqrt{S}}{S+1} + O(\alpha), \\ c_2 &= 1 + r\frac{S-1-\mathrm{i}\sqrt{S}}{S+1} + O(\alpha), \\ c_3 &= 1 - r\frac{S-1}{S+1}\alpha + O(\alpha^2). \end{aligned}$$

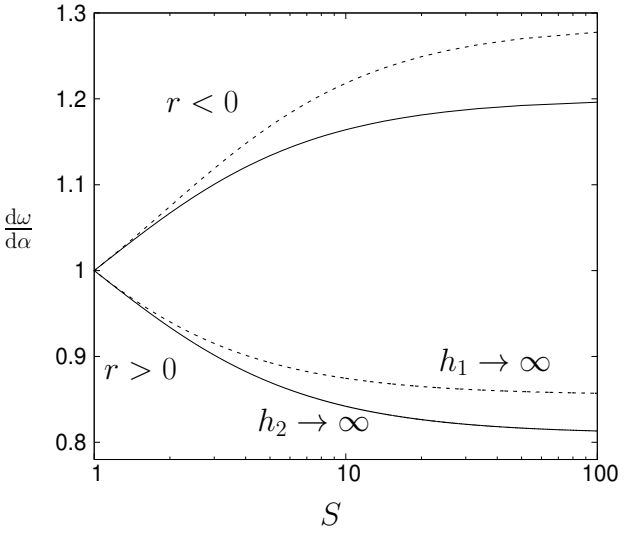

Figure 17. Plot of the group velocity $\frac{d\omega}{d\alpha}$ from (6.3) for the cases $h_2 \to \infty$ with $\alpha_0 h_1 = 1$ (solid line) and $h_1 \to \infty$ with $\alpha_0 h_2 = 1$ (dashed line) together with $\epsilon|r|\alpha_0 = 0.1$.

The key mode here is c_3 which is not present in the homogeneous case. This mode has dispersion at higher order and thus we can determine its group velocity as

$$\frac{d\omega}{d\alpha} = 1 - 2r\frac{S-1}{S+1}\alpha + O(\alpha^2). \tag{6.2}$$

Absolute instability is associated with a mode with zero group velocity at some point, and it can be seen from (6.2) that for $r > 0$ the group velocity of this mode is reduced, while for $r < 0$ the group velocity is increased, suggesting that in the unconfined problem, flows with $r > 0$ are more absolutely unstable, which is in line with the results presented in figure 15 in the far field.

But what about when confining plates are considered? If now we consider disturbances to the profile (6.1) which satisfy the boundary conditions $v(1+h_1/\epsilon) = 0$ and $v(-1-h_2/\epsilon) = 0$ with $\alpha = \epsilon\alpha_0$ and $\epsilon \ll 1$, then we find the same mode now has the form

$$c_3 = 1 - \epsilon r(S-1)\frac{\coth(\alpha_0 h_1)\coth(\alpha_0 h_2)}{\coth(\alpha_0 h_2)S + \coth(\alpha_0 h_1)}\alpha_0 + O(\epsilon^2),$$

which is again dispersive with group velocity

$$\begin{aligned}\frac{d\omega}{d\alpha} \quad = \quad & 1 - 2\epsilon r(S-1)\frac{\coth(\alpha_0 h_1)\coth(\alpha_0 h_2)}{\coth(\alpha_0 h_2)S + \coth(\alpha_0 h_1)}\alpha_0 \\ & + \epsilon r(S-1)\frac{h_1\,\mathrm{cosech}^2(\alpha_0 h_1)\coth(\alpha_0 h_2) + h_2\coth(\alpha_0 h_1)\,\mathrm{cosech}^2(\alpha_0 h_2)}{\coth(\alpha_0 h_2)S + \coth(\alpha_0 h_1)}\alpha_0^2 \\ & - \epsilon r(S-1)\frac{\coth(\alpha_0 h_1)\coth(\alpha_0 h_2)(h_1\,\mathrm{cosech}^2(\alpha_0 h_1) + Sh_2\,\mathrm{cosech}^2(\alpha_0 h_2))}{(\coth(\alpha_0 h_2)S + \coth(\alpha_0 h_1))^2}\alpha_0^2 \\ & + O(\epsilon^2). \end{aligned} \tag{6.3}$$

In figure 17 we plot (6.3) for the cases $h_2 \to \infty$ with $\alpha_0 h_1 = 1$ (solid line) and $h_1 \to \infty$ with $\alpha_0 h_2 = 1$ (dashed line) together with $\epsilon|r|\alpha_0 = 0.1$. What this figure demonstrates is that for $r > 0$ the $h_2 \to \infty$ mode is slowed more than the $h_1 \to \infty$ result and so is the

more likely to reach a point with zero group velocity first, and hence is more absolutely unstable. For $r < 0$ the opposite is true, with the $h_2 \to \infty$ mode group velocity increased less than the $h_1 \to \infty$ mode and hence is more stable. While this mechanism is consistent with the results in figures 15 and 16 it does not explain all the observations in our results, such as why the strongest destabilization was not observed in the semi-confined limit.

7. Effect of a continuous density profile

In this final section we consider the AI asymmetric properties for the tanh shear layer, but with a continuous density profile, in order to investigate whether the AI destabilizing effects of asymmetry observed for the step density profile (2.12) are robust and are equally observed for a continuous density profile. A smooth density profile is used to model a flow of two miscible fluids which includes an amount of mixing in between them.

The continuous density profile we consider is

$$\widehat{S}(y) = S + \frac{1}{2}(1 - S)\left[1 + \tanh\left(\frac{y - d}{\Delta}\right)\right], \tag{7.1}$$

where Δ is a smoothing parameter. When $\Delta \to 0$ we recover the density jump (2.12) considered before, while for $\Delta = O(1)$ we have a density profile with the same width as the shear layer. The AI properties of the flow are determined using the same approach as outlined in §5, but instead of the jump conditions (2.13) being applied, continuity conditions on v and v' are applied at $y = d$. Unlike for the density jump case, we find that we need to reduce the integration step size when solving (2.9) for cases with $\Delta < 0.5$, in order to make sure the density profile is fully resolved in the calculation.

In this section the limiting case of zero Richardson number ($F \to \infty$) does not make sense, because in this case the continuous nature of the density profile is then neglected. Hence in this section we do not consider results with $F^{-2} = 0$, and instead compare results against the results of the step-profile in §5 and §6 for nonzero $0 < F^{-2} \ll 1$. With this in mind, we note that the global temporal eigenvalues for the continuous density profile have the same qualitative structure as seen in figure 2(d). In calculations, not shown, we identify two unstable modes, one linked to the Kelvin-Helmholtz instability, and one linked to an internal mode due to the existence of the density variation. For the continuous profiles we find that these internal modes ultimately stabilize for short-wave disturbances more readily than for the density-jump case in §3. As there are similarities between the mode structures for both the continuous density profile and the density-jump profile, we expect qualitative agreement between the AI results for the two flow models.

In figure 18 we consider the neutral curve for the tanh shear layer with symmetric confinement ($h_1 = h_2 = h$) for $S = 2$ with $F^{-2} = 0.01$ and $S = 20$ with $F^{-2} = 0.001$. The results are presented for a range of smoothness parameters from $\Delta = 0$ (the density jump result) to $\Delta = 2$. The results show for both values of S that wider density profiles lead to more stable AI flow properties for all confinement values considered. In (a) ($S = 2$) the AI stability properties are due to both the unconfined and confinement saddles, and the stabilization effect observed is similar for both saddle types, i.e. the neutral curve is effectively translated up the r-axis. In (b) ($S = 20$) the neutral curve properties are due to confinement saddles only, and in this case we observe that different confinement saddles are stabilized by a different amount, however the overall qualitative effect is the same for all saddle points, they are stabilized as Δ increases.

Therefore, as the result of smoothing out the density jump is to stabilize the AI, then one question to ask is, do we still observe the region of enhanced AI for $d < 0$ with $r > 0$ with the continuous density profile? In figure 19 we investigate this question for $S = 2$ and

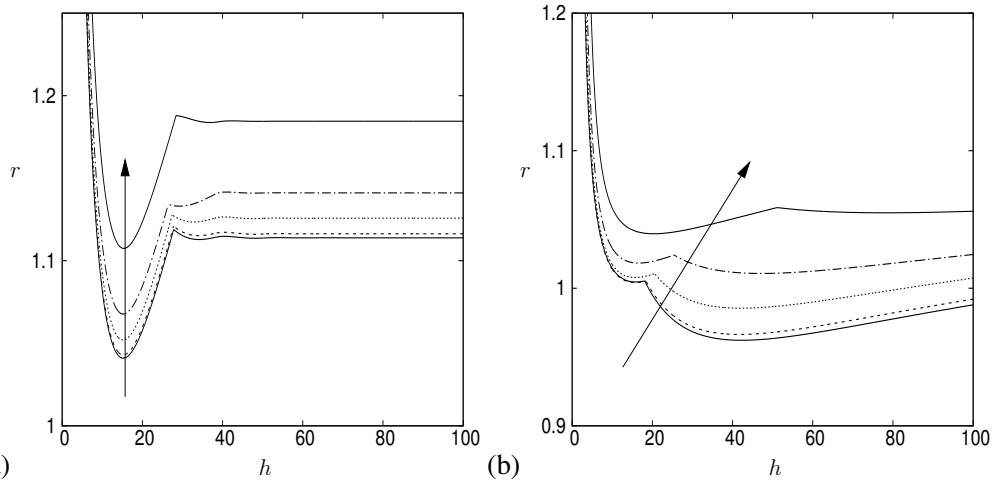

Figure 18. Plot of the neutral curves of the tanh shear layer with the continuous density profile (7.1) with symmetric confinement $h_1 = h_2 = h$ in the (h, r)-plane for $d = 0$ and (a) $(S, F^{-2}) = (2, 0.01)$ and $(S, F^{-2}) = (20, 0.001)$. The arrows indicate an increasing density smoothing parameter $\Delta = 0,\ 0.1,\ 0.5,\ 1$ and 2.

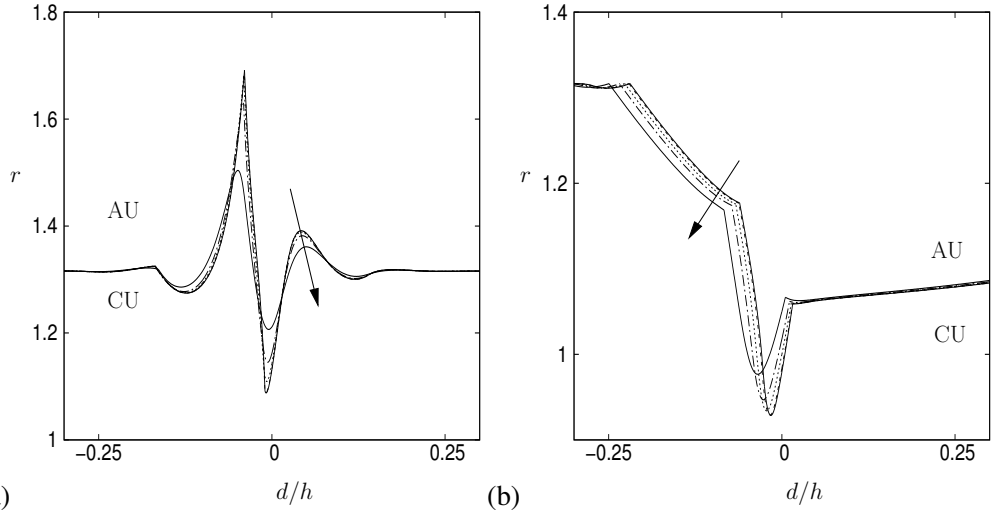

Figure 19. Plot of the neutral curves of the tanh shear layer with the continuous density profile (7.1) with symmetric confinement $h_1 = h_2 = h$ in the $(d/h, r)$-plane for $h = 100$ and (a) $(S, F^{-2}) = (2, 0.05)$ and $(S, F^{-2}) = (20, 0.0005)$. The arrows indicate an increasing density smoothing parameter $\Delta = 0,\ 0.1,\ 0.5,\ 1$ and 2.

$S = 20$. The results show that while the overall magnitude of the variations of the neutral curve reduce as Δ is increased, there is also a shift in the position of the minimum r value to a smaller value of d/h. This is most clearly seen in the $S = 20$ result in figure 19(b), and in this case the continuous density profile does actually lead to a more absolutely unstable flow at smaller values of d/h as Δ is increased. However, it is clear from these results that the main effect of the wider, continuous density profile is to *smooth out* the neutral curve, and reduce the AI for all values of d/h.

For the case where $d = 0$ with asymmetric confinement ($h_1 = Hh_2$ and $h_2 = Hh_1$ etc), figure 20 confirms the stabilizing effect of a continuous density profile for $S = 2$. The

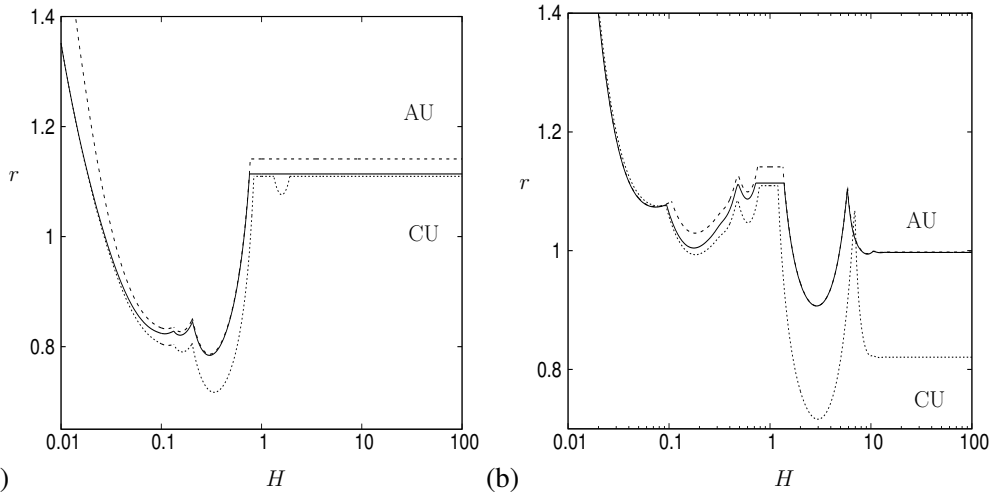

Figure 20. Plot of the neutral curves of the tanh shear layer with the continuous density profile (7.1) with $\Delta = 1$ (dashed lines) with asymmetric confinement in the (H, r)-plane for $(S, F^{-2}) = (2, 0.01)$ and (a) $h_1 = Hh_2$ with $h_2 = 100$ and (b) $h_2 = Hh_1$ with $h_1 = 100$. The solid lines correspond to the discontinuous density profile with $F^{-2} = 0.01$, and the lower dotted lines are the corresponding $F^{-2} = 0$ results from figures 12(a) and 13(a).

variation is maximal for $H < 1$ because in this case the variable plate is moving closer to the shear layer. The continuous profile results follow the discontinuous profile results well at the global minimums of the two neutral curves and hence the instability of asymmetric confinement on the AI for inhomogeneous shear flows is still observed. Therefore, the results of this section demonstrate that the AI effects observed due to asymmetry for the discontinuous density profile are robust and are qualitatively similar for continuous density profiles. These results also show that the case $F^{-2} \neq 0$ for the asymmetric confinement case can have a significant effect on the values of minimum r on the neutral curve, particularly for the case when the lower plate position is varied in figure 20(b).

8. Conclusions

In this paper we consider the effects of asymmetric confinement and asymmetrically centered density profiles on the stability properties of an inhomogeneous shear layer with a stable vertical stratification. The major focus of the results is on high-speed flows such that the Richardson number, $\widehat{S}'F^{-2}/\widehat{S}$, which is a measure of the effect of buoyancy, is small, with the $F^{-2} = 0$ case considered as a limiting case. When $F^{-2} = 0$ (zero gravity) the confinement effect on the temporal stability takes one of two cases. When the velocity profile has $d > 0$, where d is the point at which there is a jump in density from 1 to S, the inflection point of the shear layer lies in the heavier of the two fluids. In this case the flow is shown to have a single pair of complex conjugate temporal eigenvalues, ω, which eventually stabilize beyond some critical wavenumber α and are consistent with Kelvin-Helmholtz shear modes. For these modes, semi-confinement (confinement by a single plate) has the weakest stabilizing effect, symmetric confinement is more stabilizing and asymmetric confinement the most stabilizing, except for a small range of flow parameters, when $r < 0$ (where r is the shear rate), where symmetric confinement is most stabilizing. In each case the shape of the neutral curve is independent of the magnitude of the shear rate r and asymptotes to the unconfined result exponentially fast as the plates move away from the shear layer. Thus giving the commonly held belief that, as long as the plates

are far enough away, the effect of confinement can be ignored. When $d \leq 0$, then the inflection point of the shear layer lies in the lighter of the two fluids and there exists two pairs of complex conjugate eigenvalues, one Kelvin-Helmholtz pair again, and a second pair related to internal modes which are concentrated at the density layer. In this case the Kelvin-Helmholtz mode again stabilizes for large wavenumbers, while the internal mode gives rise to an instability which persists for all wavenumbers, and hence there is no neutral curve to calculate. When $F^{-2} \neq 0$, the internal modes can be shown to exist even for the case $d > 0$, and while these modes remain unstable for large wavenumbers, they eventually do stabilize and produce a neutral curve. However, these modes are confined to a region close to the density change, and as such their stability properties are not affected by symmetric or asymmetric confinement.

When we consider the asymmetric effects of confinement and the fluid interface position on the absolute instability characteristics of the flow, we find a contrasting position where the asymmetric case can lead to a strong destabilizing effect. This effect can remain strong even when the plates are far from the shear layer, where intuition tells us that the unconfined result should be achieved. The strongest destabilizing effect was found for $h_2/h_1 = H(S)$ with $r > 0$, where $-h_2$ is the plate position in the slower stream and h_1 is the plate position in the faster stream. We found H to be an increasing function of S with $H = 2.53$ for $S = 1$. For $S = 1$ Healey (2009) found a co-flow ($|r| < 1$) absolute instability for $2.35 < H < 2.72$, and for $F^{-2} = 0$ we find this region increases dramatically for the inhomogeneous case, with a co-flow absolute instability for $1.28 < H < 37.04$ for $S = 2$, when $h_2 = 100$ is fixed, and $1.28 < H < 6.48$ and $H > 7.15$ for $S = 2$ when $h_1 = 100$ is fixed, for example. Thus, whether the flow is confined in the faster or slower of the two streams is significant to the AI properties of the flow.

The effect of varying the fluid interface position from $d = 0$ in a symmetrically confined system ($h = h_1 = h_2$) is found to generally have a stabilizing effect on the absolute instability, except for a small region of $d/h < 0$ where a destabilizing effect, weaker than the asymmetric confinement effect, is identified. The size of this region and the magnitude of the effect depend on the value of S, where for $S = 2$, $-0.002 < d/h < 0$ with $r_{\min} = 1.10$ ($r(d = 0) = 1.11$) and for $S = 100$, $-0.0175 < d/h < 0$ with $r_{\min} = 0.9913$ ($r(d = 0) = 0.9951$), when $F^{-2} = 0$.

The presented results are compared with the long-wave theory, in which the specific details of the shear layer profile are not present, and the flow can be modelled as a piecewise linear flow. For large density ratios $S \geq 20$, the long-wave theory provides good agreement with the full numerical results, especially in the cases of asymmetric confinement.

Semi-confinement can be considered as the limiting case of asymmetric confinement when h_1 or $h_2 \to \infty$ with the corresponding h_2 or h_1 finite. For semi-confinement we find that placing the plate in the faster and lighter fluid leads to the most unstable absolute instability scenario with most density ratios with $S > 1$ having co-flow absolute instabilities for the majority of plate positions, h_1. The most stable configuration has the plate in the slower lighter fluid where, in this case, a large counter-flow is required to generate an absolute instability. Therefore using a single plate to confine the flow could be a suitable mechanism for suppressing an absolute instability in shear layers.

The results in this paper are presented for an inviscid flow, but in most experimental scenarios viscosity will be important. As discussed in §2.1 the effect of boundary layers at the bounding plates only become significant for strong confinements $h_1, h_2 \lesssim 2$ (Juniper *et al.* 2011) and so the results presented here should not be affected by this. Where viscosity might be more significant is in modifying the purely anti-symmetric velocity and density profiles. Healey (2009) showed for the homogeneous shear layer that carefully chosen asymmetric velocity profiles can enhance the AI, but it is equally true that other

less-carefully chosen profiles could diminish the AI. In this case it is not clear without numerically calculating the base flow, whether the asymmetric forms of the velocity and density profiles would enhance or diminish the AI, and in particular whether the enhanced AI seen for cases where $d < 0$ would be removed. Given the large AI effect of the asymmetric confinement, we would expect this enhancement effect to still be evident for small base flow asymmetries. This inclusion of viscosity could be considered in future work. Another possible element of future work might be to consider the effect of flexible compliant plates on controlling the AI. Poole & Turner (2023, 2024) showed for a parallel jet/wake flow that the inclusion of compliant plates introduced new instability modes, due to the flexibility of the plate, into the problem which can introduce AI into flow scenarios, which with rigid plates are only convectively unstable.

Acknowledgements. This research was funded in part, by the Engineering and Physical Sciences Research Council via grant numbers EP/W006545/1 and UKRI070. For the purpose of Open Access, the author has applied a Creative Commons Attribution (CC BY) public copyright licence to any Author Accepted Manuscript version arising from this submission. MT would like to thank the anonymous referees whose comments have led to a significantly improved manuscript.

Declaration of interests. The authors report no conflict of interest.

Author ORCIDs. M. R. Turner, https://orcid.org/0000-0002-1680-755X

References

Anni, L. & Farmer, D. M. 1988 The flow of Mediterranean water through the strait of Gibraltar. *Prog. Oceanogr.* **21** (1).

Bozonnet, C., Matas, J.-P., Balarac, G. & Desjardins, O. 2022 Stability of an air–water mixing layer: focus on the confinement effect. *J. Fluid Mech.* **933**, A14.

Brambley, E. 2010 A well-posed modified myers boundary condition. In *16th AIAA/CEAS Aeroacoustics Conference*, p. 3942.

Briggs, R. J. 1964 *Electron–Stream Interaction with Plasmas*. MIT Press.

Carpenter, J. R., Balmforth, N. J. & Lawrence, G. A. 2010 Identifying unstable modes in stratified shear layers. *Phys. Fluids* **22** (5).

Caulfield, C. P. 2021 Layering, instabilities, and mixing in turbulent stratified flows. *Annu. Rev. Fluid Mech.* **53** (1), 113–145.

Caulfield, C. P., Peltier, W. R., Yoshida, S. & Ohtani, M. 1995 An experimental investigation of the instability of a shear flow with multilayered density stratification. *Phys. Fluids* **7** (12), 3028–3041.

Danyi, R. 2018 Global instability of mixing layers created by confinement. PhD thesis, University of Keele.

Drazin, P. G. 2002 *Introduction to Hydrodynamic Stability*, , vol. 32. Cambridge university press.

Drazin, P. G. & Reid, W. H. 1981 *Hydrodynamic Stability*. Cambridge University Press.

Garrett, S. J. & Peake, N. 2007 The absolute instability of the boundary layer on a rotating cone. *Eur. J. Mech. B Fluids* **26** (3), 344–353.

Healey, J. J. 2006*a* Inviscid long-wave theory for the absolute instability of the rotating-disc boundary layer. *Proc. R. Soc. Lond. A* **462** (2069), 1467–1492.

Healey, J. J. 2006*b* A new convective instability of the rotating-disk boundary layer with growth normal to the disk. *J. Fluid Mech.* **560**, 279–310.

Healey, J. J. 2007 Enhancing the absolute instability of a boundary layer by adding a far-away plate. *J. Fluid Mech.* **579**, 29–61.

Healey, J. J. 2008 Inviscid axisymmetric absolute instability of swirling jets. *J. Fluid Mech.* **613**, 1–33.

Healey, J. J. 2009 Destabilizing effects of confinement on homogeneous mixing layers. *J. Fluid Mech.* **623**, 241–271.

Helmholtz, H. 1868 On discontinuous movements of fluids. *London, Edinburgh and Dublin Philos. Mag. J. Sci.* **36** (244), 337–346.

Homma, S., Koga, J., Matsumoto, S., Song, M. & Tryggvason, G. 2006 Breakup mode of an axisymmetric liquid jet injected into another immiscible liquid. *Chem. Eng. Sci.* **61** (12), 3986–3996.

Huerre, P. & Monkewitz, P. A. 1985 Absolute and convective instabilities in free shear layers. *J. Fluid Mech.* **159**, 151–168.

Huerre, P. & Monkewitz, P. A. 1990 Local and global instabilities in spatially developing flows. *A. Rev. Fluid Mech.* **22**, 473–537.

Juniper, M. P. 2006 The effect of confinement on the stability of two-dimensional shear flows. *J. Fluid Mech.* **565**, 171–195.

Juniper, M. P. 2007 The full impulse response of two-dimensional jet/wake flows and implications for confinement. *J. Fluid Mech.* **590**, 163–185.

Juniper, M. P. 2008 The effect of confinement on the stability of non-swirling round jet/wake flows. *J. Fluid Mech.* **605**, 227–252.

Juniper, M. P. & Candel, S. M. 2003 The stability of ducted compound flows and consequences for the geometry of coaxial injectors. *J. Fluid Mech.* **482**, 257–269.

Juniper, M. P., Tammisola, O. & Lundell, F. 2011 The local and global stability of confined planar wakes at intermediate Reynolds number. *J. Fluid Mech.* **686**, 218–238.

Kelvin, W. 1871 Hydrokinetic solutions and observations. *London, Edinburgh and Dublin Philos. Mag. J. Sci.* **42** (281), 362–377.

Kitamura, Y., Mishima, H. & Takahashi, T. 1982 Stability of jets in liquid-liquid systems. *Can. J. Chem. Eng.* **60** (6), 723–731.

Koop, C. G. & Browand, F. K. 1979 Instability and turbulence in a stratified fluid with shear. *J. Fluid Mech.* **93** (1), 135–159.

Lasheras, J. C., Villermaux, E. & Hopfinger, E. J. 1998 Break-up and atomization of a round water jet by a high-speed annular air jet. *J. Fluid Mech.* **357**, 351–379.

Lawrence, G. A., Browand, F. K. & Redekopp, L. G. 1991 The stability of a sheared density interface. *Phys. Fluids A* **3** (10), 2360–2370.

Le Dizès, S. & Billant, P. 2009 Radiative instability in stratified vortices. *Phys. Fluids* **21** (9).

Lefebvre, A. H. & McDonell, V. G. 2017 *Atomization and sprays*. CRC press.

Lim, D. W. & Redekopp, L. G. 1998 Absolute instability conditions for variable density, swirling jet flows. *Eur. J. Mech. B/Fluids* **17** (2), 165–185.

Matas, J.-P. 2015 Inviscid versus viscous instability mechanism of an air–water mixing layer. *J. Fluid Mech.* **768**, 375–387.

Matas, J.-P., Delon, A. & Cartellier, A. 2018 Shear instability of an axisymmetric air–water coaxial jet. *J. Fluid Mech.* **843**, 575–600.

Michalke, A. 1964 On the inviscid instability of the hyperbolic-tangent velocity profile. *J. Fluid Mech.* **19** (4), 543–556.

Ouro, Pablo, Muhawenimana, Valentine & Wilson, Catherine AME 2019 Asymmetric wake of a horizontal cylinder in close proximity to a solid boundary for Reynolds numbers in the subcritical turbulence regime. *Phys. Rev. Fluids* **4** (10), 104604.

Peltier, W. R. & Caulfield, C. P. 2003 Mixing efficiency in stratified shear flows. *Annu. Rev. Fluid Mech.* **35** (1), 135–167.

Pier, B. & Peake, N. 2015 Global modes with multiple saddle points. *Eur. J. Mech. B Fluids* **49**, 335–344.

Poole, R. & Turner, M. R. 2023 Stability of jets and wakes confined by compliant walls. *Phys. Rev. Fluids* **8** (6), 063901.

Poole, R. & Turner, M. R. 2024 The effect of asymmetry on the absolute instability of confined jets and wakes. *Fluid Dyn. Res.* **56** (5), 055504.

Pouliquen, O., Chomaz, J. M. & Huerre, P. 1994 Propagating Holmboe waves at the interface between two immiscible fluids. *J. Fluid Mech.* **266**, 277–302.

Rayleigh, J. W. S. B. 1896 *The Theory of Sound*, , vol. 2. Macmillan.

Richards, J. R., Lenhoff, A. M. & Beris, A. N. 1994 Dynamic breakup of liquid–liquid jets. *Phys. Fluids* **6** (8), 2640–2655.

Riedinger, X., Le Dizès, S. & Meunier, P. 2010 Viscous stability properties of a lamb–oseen vortex in a stratified fluid. *J. Fluid Mech.* **645**, 255–278.

Rienstra, S. W. & Darau, M. 2011 Boundary-layer thickness effects of the hydrodynamic instability along an impedance wall. *J. Fluid Mech.* **671**, 559–573.

Schmid, P. J. & Henningson, D. S. 2001 *Stability and Transition in Shear Flows*. Springer .

Sirignano, W. A. 2021 Mixing and combustion in a laminar shear layer with imposed counterflow. *J. Fluid Mech.* **908**, A35.

Strykowski, P. J. & Niccum, D. L. 1992 The influence of velocity and density ratio on the dynamics of spatially developing mixing layers. *Phys. Fluids A* **4** (4), 770–781.

Tammisola, O. & Juniper, M. P. 2016 Coherent structures in a swirl injector at Re= 4800 by nonlinear simulations and linear global modes. *J. Fluid Mech.* **792**, 620–657.

Tammisola, O., Lundell, F., Schlatter, P., Wehrfritz, A. & Söderberg, L. D. 2011 Global linear and nonlinear stability of viscous confined plane wakes with co-flow. *J. Fluid Mech.* **675**, 397–434.

Taylor, M. J. & Peake, N. 1999 A note on the absolute instability of wakes. *Eur. J. Mech. B Fluids* **18** (4), 573–579.

Tedford, E. W., Carpenter, J. R., Pawlowicz, R., Pieters, R. & Lawrence, G. A. 2009 Observation and analysis of shear instability in the fraser river estuary. *J. Geophys. Res.* **114** (C11).

Triantafyllou, G. S. 1994 Note on the Kelvin–Helmholtz instability of stratified fluids. *Phys. Fluids* **6** (1), 164–171.

Weilgart, L. 2018 The impact of ocean noise pollution on fish and invertebrates. *Report for OceanCare, Switzerland* .

Wesson, J. C. & Gregg, M. C. 1994 Mixing at Camarinal sill in the Strait of Gibraltar. *J. Geophys. Res.* **99** (C5), 9847–9878.

Yoshida, S., Ohtani, M., Nishida, S. & Linden, P. F. 1998 Mixing processes in a highly stratified river. *Physical Processes in Lakes and Oceans* **54**, 389–400.

Yu, M.-H. & Monkewitz, P. A. 1990 The effect of nonuniform density on the absolute instability of two-dimensional inertial jets and wakes. *Phys. Fluids A* **2** (7), 1175–1181.

Zuccoli, E., Brambley, E. J. & Barkley, D. 2024 Trapped free surface waves for a lamb–oseen vortex flow. *J. Fluid Mech.* **997**, A40.